Measurement of the shape of the $B_s^0 \to D_s^{*-}\mu^+\nu_\mu$ differential decay rate

The LHCb collaboration

E-mail: rvazquez@cern.ch

Abstract: The shape of the $B_s^0 \to D_s^{*-}\mu^+\nu_\mu$ differential decay rate is obtained as a function of the hadron recoil parameter using proton-proton collision data at a centre-of-mass energy of 13 TeV, corresponding to an integrated luminosity of $1.7\,\text{fb}^{-1}$ collected by the LHCb detector. The $B_s^0 \to D_s^{*-}\mu^+\nu_\mu$ decay is reconstructed through the decays $D_s^{*-} \to D_s^-\gamma$ and $D_s^- \to K^-K^+\pi^-$. The differential decay rate is fitted with the Caprini-Lellouch-Neubert (CLN) and Boyd-Grinstein-Lebed (BGL) parametrisations of the form factors, and the relevant quantities for both are extracted.

Contents

1   Introduction

Semileptonic decays of heavy hadrons are commonly used to measure the parameters of the Cabibbo-Kobayashi-Maskawa (CKM) matrix [1, 2], as they involve only one hadronic current that can be parametrised in terms of scalar functions known as form factors. The number of form factors needed to describe a particular decay depends upon the spin of the initial- and final-state hadrons [3–5]. For the decay of a pseudoscalar B meson to a vector

D^* meson, four form factors are required. The determination of the CKM matrix element $|V_{cb}|$ using $B \to D^{(*)}\ell\nu_\ell$ decays or via the inclusive sum of all hadronic $B \to X_c\ell\nu_\ell$ decay channels has been giving inconsistent results during the last thirty years [6]. The exclusive determination relies heavily on the parametrisation of the form factors, as it requires an extrapolation of the differential decay rate to the zero recoil point, where the momentum transfer to the lepton system is maximum.

Recently, the LHCb collaboration has measured $|V_{cb}|$ using $B_s^0 \to D_s^{(*)-}\mu^+\nu_\mu$ decays[1] with two form-factor parametrisations, giving consistent results [7]. The determination of the form factors in $B_s^0 \to D_s^{*-}\ell^+\nu_\ell$ decays obtained using different parametrisations can help to clarify the $|V_{cb}|$ inconsistency between the exclusive and inclusive approaches. It can also be used to improve the Standard Model (SM) predictions of the $B_s^0 \to D_s^{*-}\tau^+\nu_\tau$ branching fraction and the ratio $\mathcal{R}(D_s^*) = \mathcal{B}(B_s^0 \to D_s^{*-}\tau^+\nu_\tau)/\mathcal{B}(B_s^0 \to D_s^{*-}\mu^+\nu_\mu)$. A measurement and precise prediction of the latter could increase the understanding of the current tension between experimental and theoretical values of the equivalent ratio $\mathcal{R}(D^{(*)}) = \mathcal{B}(B \to D^{(*)}\tau^+\nu_\tau)/\mathcal{B}(B \to D^{(*)}\mu^+\nu_\mu)$ [6]. Theoretical predictions on B_s^0 semileptonic decays are expected to be more precise than those on B^0 or B^+ decays. For example, the Lattice QCD calculations of the form factors are computationally easier due to the larger mass of the spectator s quark compared to that of u or d quarks [8, 9]. Despite these advantages, the study of semileptonic B_s^0 decays has received less theoretical attention than the equivalent B^0 and B^+ decays due to the lack of experimental results.

This paper reports the first measurement of the shape of the differential decay rate of the $B_s^0 \to D_s^{*-}\mu^+\nu_\mu$ decay as a function of the hadronic recoil parameter $w = v_{B_s^0} \cdot v_{D_s^{*-}}$, where $v_{B_s^0}$ and $v_{D_s^{*-}}$ are the four-vector velocities of the B_s^0 and D_s^{*-} mesons, respectively. The spectrum of w is unfolded accounting for the detector resolution on w and corrected for the reconstruction and selection efficiency. The D_s^{*-} meson is reconstructed in the $D_s^{*-} \to D_s^-\gamma$ mode, where the D_s^- meson subsequently decays via the $D_s^- \to \phi(\to K^+K^-)\pi^-$ or $D_s^- \to K^{*0}(\to \pi^-K^+)K^-$ mode. The data used correspond to an integrated luminosity of $1.7\,\mathrm{fb}^{-1}$ collected by the LHCb experiment in 2016 at a centre-of-mass energy of $13\,\mathrm{TeV}$.

The $B_s^0 \to D_s^{*-}\mu^+\nu_\mu$ decay is described by four form factors. The most commonly used parametrisations to model these form factors are by Caprini-Lellouch-Neubert (CLN) [10] and by Boyd-Grinstein-Lebed (BGL) [11–13]. This paper also describes how the relevant parameters of these parametrisations can be extracted by fitting the measured differential decay rate.

2 Formalism of the $B_s^0 \to D_s^{*-}\mu^+\nu_\mu$ decay

The $B_s^0 \to D_s^{*-}\mu^+\nu_\mu$ decay, with the subsequent $D_s^{*-} \to D_s^-\gamma$ decay, can be described by three angular variables and the squared momentum transfer to the lepton system, defined as $q^2 = (p_{B_s^0} - p_{D_s^{*-}})^2$, where $p_{B_s^0}$ and $p_{D_s^{*-}}$ are the four-momenta of the B_s^0 and D_s^{*-} mesons, respectively. The three angular variables, indicated in figure 1, are two helicity angles θ_μ and θ_{D_s}, and the angle χ. In this figure the direction of the z-axis is defined in the

---
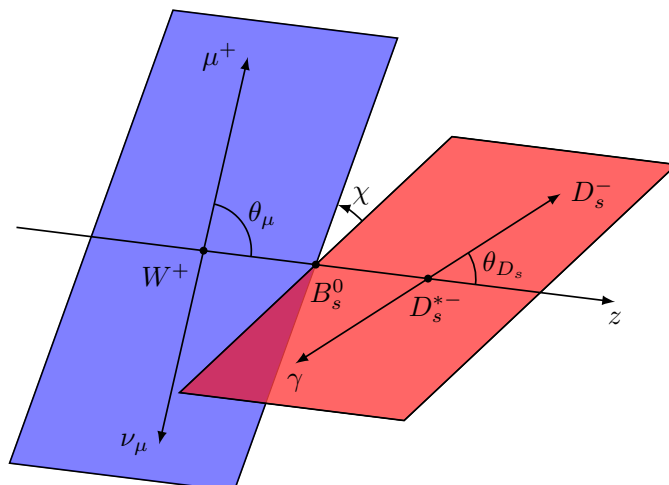[1]The inclusion of charge-conjugate processes is implied throughout this paper.

Figure 1. Schematic overview of the $B_s^0 \to D_s^{*-} \mu^+ \nu_\mu$ decay, introducing the angles θ_{D_s}, θ_μ and χ.

B_s^0 rest frame as $\hat{z} = \vec{p}_{D_s^{*-}}/|\vec{p}_{D_s^{*-}}|$. The angle between the muon direction in the virtual W rest frame and the z direction is called θ_μ, while the angle between the D_s^- meson direction in the D_s^{*-} rest frame and the z direction is called θ_{D_s}. Finally, χ is the angle between the plane formed by the D_s^{*-} decay products and that formed by the two leptons in the B_s^0 rest frame [14]. The angular basis is designed such that the angular definition for the $\bar{B}_s^0$ decay is a CP transformation of that of the B_s^0 decay.

The measurement is performed by integrating the full decay rate over the decay angles. Thus, the expression of the $B_s^0 \to D_s^{*-} \mu^+ \nu_\mu$ decay rate is given by

$$
\frac{\mathrm{d}\Gamma(B_s^0 \to D_s^{*-} \mu^+ \nu_\mu)}{\mathrm{d}q^2} = \frac{G_{\mathrm{F}}^2 \, |V_{cb}|^2 \, |\eta_{\mathrm{EW}}|^2 \, |\vec{p}| q^2}{96 \, \pi^3 \, m_{B_s^0}^2} \left(1 - \frac{m_\mu^2}{q^2}\right)^2
$$
$$
\times \left[(|H_+|^2 + |H_-|^2 + |H_0|^2) \left(1 + \frac{m_\mu^2}{2\,q^2}\right) + \frac{3}{2}\frac{m_\mu^2}{q^2}|H_t|^2 \right].
$$
(2.1)

In this equation, G_{F} is the Fermi constant, V_{cb} is the CKM matrix element describing the b to c transition, $\eta_{\mathrm{EW}} = 1.0066$ is the electroweak correction to V_{cb} [15], m_μ is the muon mass [16], and H_0, H_+, H_-, H_t are the helicity amplitudes. The magnitude of the D_s^{*-} momentum in the B_s^0 rest frame is given by $|\vec{p}|$. The hadronic recoil, w, is related to the squared momentum transfer to the lepton pair, q^2, by

$$
w = \frac{p_{B_s^0}}{m_{B_s^0}} \cdot \frac{p_{D_s^{*-}}}{m_{D_s^{*-}}} = \frac{m_{B_s^0}^2 + m_{D_s^{*-}}^2 - q^2}{2\,m_{B_s^0}\,m_{D_s^{*-}}},
$$
(2.2)

where $m_{B_s^0}$ and $m_{D_s^{*-}}$ are the masses of the B_s^0 and D_s^{*-} mesons, respectively. The minimal value, $w = 1$, corresponds to the situation in which the D_s^{*-} meson has zero recoil in the B_s^0 rest frame. It is also the value for which q^2 is maximal.

The dependence of the helicity amplitudes on w can be expressed in different ways, most commonly described in either the CLN or BGL parametrisations, as discussed further

in section 2.1 and section 2.2. This analysis is only sensitive to a single form-factor contribution while the other form factors are fixed to existing measurements from B^+ and B^0 semileptonic decays [6, 17]. This is supported by ref. [18], where when imposing unitarity and analyticity the differences in form factors for semileptonic $B \to D$ and $B_s^0 \to D_s^+$ decays are found to be within $\mathcal{O}(1\%)$ over the entire kinematic range. Also, a simultaneous analysis of the $B_q \to D_q^{(*)}$ form factors for both light ($q = u, d$) and strange ($q = s$) spectator quarks within the Heavy-Quark-Expansion framework to order $\mathcal{O}(\alpha_s, 1/m_b, 1/m_c^2)$ [19] does not show any significant SU(3) symmetry breaking. Moreover, Lattice QCD calculations indicate that there is also good agreement of the form factors at zero recoil [9, 20].

2.1 CLN form-factor parametrisation

For the CLN parametrisation [10], the helicity amplitudes H_0, H_+, H_- and H_t can be written in terms of the form factors $A_1(w)$, $V(w)$, $A_2(w)$ and $A_0(w)$ as

$$
\begin{aligned}
H_\pm(w) &= m_{B_s^0}\,(1+r)\,A_1(w) \mp \frac{2}{1+r}\,|\vec{p}|\,V(w), \\
H_0(w) &= \frac{m_{B_s^0}\,m_{D_s^{*-}}\,(w-r)\,(1+r)^2\,A_1(w) - 2\,|\vec{p}|^2\,A_2(w)}{m_{D_s^{*-}}\,(1+r)\,\sqrt{1+r^2-2wr}}\,, \\
H_t(w) &= \frac{2\,|\vec{p}|}{\sqrt{1+r^2-2wr}}\,A_0(w)\,,
\end{aligned}
\tag{2.3}
$$

where $r = m_{D_s^{*-}}/m_{B_s^0}$. The form factors are rewritten in terms of a single leading form factor

$$
h_{A_1}(w) = A_1(w)\frac{1}{R_{D_s^{*-}}}\frac{2}{w+1}\,,
\tag{2.4}
$$

and three ratios of form factors

$$
R_0(w) = \frac{A_0(w)}{h_{A_1}(w)}R_{D_s^{*-}}\,, \qquad R_1(w) = \frac{V(w)}{h_{A_1}(w)}R_{D_s^{*-}}\,, \qquad R_2(w) = \frac{A_2(w)}{h_{A_1}(w)}R_{D_s^{*-}}\,, \tag{2.5}
$$

where

$$
R_{D_s^{*-}} = \frac{2\sqrt{r}}{1+r}.
\tag{2.6}
$$

In the CLN parametrisation, the leading form factor and the three ratios are parametrised in terms of w as

$$
\begin{aligned}
h_{A_1}(w) &= h_{A_1}(1)[1 - 8\rho^2 z(w) + (53\rho^2 - 15)z^2(w) - (231\rho^2 - 91)z^3(w)]\,, \\
R_0(w) &= R_0(1) - 0.11(w-1) + 0.01(w-1)^2\,, \\
R_1(w) &= R_1(1) - 0.12(w-1) + 0.05(w-1)^2\,, \\
R_2(w) &= R_2(1) + 0.11(w-1) - 0.06(w-1)^2\,,
\end{aligned}
\tag{2.7}
$$

where the coefficients, originally calculated for B decays, are assumed to be the same for B_s^0 decays. The function $z(w)$ is defined as

$$
z(w) = \frac{\sqrt{w+1}-\sqrt{2}}{\sqrt{w+1}+\sqrt{2}}.
\tag{2.8}
$$

As this analysis is only sensitive to the shape of the form-factor parametrisation the term $h_{A_1}(1)$ is absorbed in the normalisation. The values of $R_1(1)$ and $R_2(1)$ are taken from the HFLAV average of the corresponding parameters, obtained from $B \to D^* \ell \nu_\ell$ decays [6]. The $R_0(1)$ parameter is suppressed by m_ℓ^2/q^2 in the helicity amplitude and its contribution to the total rate is negligible. The value predicted by the exact heavy quark limit of $R_0(1) = 1$ [21] is used, as no measurement of $R_0(1)$ has been performed. The slope, ρ^2, of $h_{A_1}(w)$ is the only parameter fitted in this parametrisation.

2.2 BGL form-factor parametrisation

In the BGL parametrisation [11–13], the helicity amplitudes are parametrised as

$$
\begin{aligned}
H_0(w) &= \frac{\mathcal{F}_1(w)}{m_{B_s^0}\sqrt{1+r^2+2wr}}\,, \\
H_\pm(w) &= f(w) \mp m_{B_s^0}\, m_{D_s^{*-}}\sqrt{w^2-1}\, g(w)\,, \\
H_t(w) &= m_{B_s^0}\frac{\sqrt{r}(1+r)\sqrt{w^2-1}}{\sqrt{1+r^2-2wr}}\mathcal{F}_2(w)\,,
\end{aligned}
\tag{2.9}
$$

where the form factors are defined as

$$
\begin{aligned}
f(z) &= \frac{1}{P_{1+}(z)\phi_f(z)}\sum_{n=0}^{\infty} a_n^f z^n\,, &\qquad \mathcal{F}_1(z) &= \frac{1}{P_{1+}(z)\phi_{\mathcal{F}_1}(z)}\sum_{n=0}^{\infty} a_n^{\mathcal{F}_1} z^n\,, \\
g(z) &= \frac{1}{P_{1-}(z)\phi_g(z)}\sum_{n=0}^{\infty} a_n^g z^n\,, &\qquad \mathcal{F}_2(z) &= \frac{\sqrt{r}}{(1+r)P_{0-}(z)\phi_{\mathcal{F}_2}(z)}\sum_{n=0}^{\infty} a_n^{\mathcal{F}_2} z^n\,.
\end{aligned}
\tag{2.10}
$$

The functions ϕ_i are the so-called outer functions, $P_{1\pm,0-}$ are Blaschke factors, and the coefficients a_n^i, where $i = \{f, g, \mathcal{F}_1, \mathcal{F}_2\}$, are parameters to be fit from data.

As the form-factor parametrisation is given through analytic functions, they must satisfy the unitarity condition in the z expansion

$$
\sum_{n=0}^{\infty}(a_n^g)^2 \le 1\,, \qquad \sum_{n=0}^{\infty}(a_n^f)^2 + \sum_{n=0}^{\infty}(a_n^{\mathcal{F}_1})^2 \le 1\,, \qquad \sum_{n=0}^{\infty}(a_n^{\mathcal{F}_2})^2 \le 1.
\tag{2.11}
$$

This analysis is only sensitive to the form factor $f(z)$, and its series is truncated at $n = 2$, following refs. [17, 22–25]. The shapes for $\mathcal{F}_1(z)$ and $g(z)$ are constrained using the results in ref. [17], where the a_n^i coefficients are fit using recent Belle measurements with $B^0 \to D^{*-}\ell^+\nu_\ell$ decays [26, 27]. The value of a_0^f in ref. [17] is determined from the combination of lattice calculations in ref. [28]. The parameters $a_n^{\mathcal{F}_2}$ for $\mathcal{F}_2(z)$ are fixed from predictions in ref. [24], where they are called P_1. As this analysis represents the first measurement of form factors in $B_s^0 \to D_s^{*-}$ transitions, the choice of the input parameters is driven by having as much experimental input as possible. An overview of the fit inputs is given in table 8 in appendix C.

3 Detector and simulation

The LHCb detector [29, 30] is a single-arm forward spectrometer covering the pseudorapidity range $2 < \eta < 5$, designed for the study of particles containing b or c

quarks. The detector includes a high-precision tracking system consisting of a silicon-strip vertex detector surrounding the pp interaction region [31], a large-area silicon-strip detector located upstream of a dipole magnet with a bending power of about 4 Tm, and three stations of silicon-strip detectors and straw drift tubes [32] placed downstream of the magnet. The tracking system provides a measurement of the momentum, p, of charged particles with a relative uncertainty that varies from 0.5% at low momentum to 1.0% at 200 GeV/c. The minimum distance of a track to a primary vertex (PV), the impact parameter (IP), is measured with a resolution of $(15 + 29/p_{\rm T})$ μm, where $p_{\rm T}$ is the component of the momentum transverse to the beam, in GeV/c. Different types of charged hadrons are distinguished using information from two ring-imaging Cherenkov detectors [33]. Photons, electrons and hadrons are identified by a calorimeter system consisting of scintillating-pad and preshower detectors, an electromagnetic and a hadronic calorimeter. Muons are identified by a system composed of alternating layers of iron and multiwire proportional chambers [34]. The online event selection is performed by a trigger [35], which consists of a hardware stage, based on information from the calorimeter and muon systems, followed by a software stage, which applies a full event reconstruction. The hardware muon trigger selects events containing a high-$p_{\rm T}$ muon candidate. The software trigger requires three tracks with a significant displacement from any primary pp interaction vertex.

Simulation is required to model the effects of the detector acceptance and the imposed selection requirements. In the simulation, pp collisions are generated using PYTHIA [36, 37] with a specific LHCb configuration [38]. Decays of unstable particles are described by EVTGEN [39], in which final-state radiation is generated using PHOTOS [40]. The interaction of the generated particles with the detector, and its response, are implemented using the GEANT4 toolkit [41, 42] as described in ref. [43].

The simulation is corrected for mismodeling of the kinematic properties of the generated B_s^0 mesons and of the photons from the D_s^{*-} decays, as well as for data-simulation differences in the muon trigger efficiency and tracking efficiencies of the final-state particles. Corrections to the B_s^0 and γ kinematic distributions are determined by comparing data and simulated samples of $B^+ \to J/\psi K^+$ and $B_s^0 \to D_s^{*-}\pi^+$ decays, respectively. Kinematic differences between B_s^0 and B^+ mesons due to their production mechanisms are small and considered to be negligible [44, 45]. Corrections to the trigger and tracking efficiencies are evaluated using data and simulated samples of $B^+ \to J/\psi K^+$ decays [46]. In the simulated signal sample, the form factors are described following the CLN parametrisation with numerical values $\rho^2 = 1.205$, $R_1(1) = 1.404$ and $R_2(1) = 0.854$.

4 Data selection

Candidate $B_s^0 \to D_s^{*-}\mu^+\nu_\mu$ decays are selected by pairing D_s^{*-} and μ^+ candidates, where the D_s^{*-} candidate is reconstructed through the $D_s^-\gamma$ decay. The D_s^- mesons are reconstructed requiring two opposite-sign kaons and a pion inconsistent with coming from a PV, and forming a common vertex that is displaced from every PV. The final-state hadrons and muon must satisfy strict particle identification (PID) criteria, consistent with the assigned particle hypothesis.

To suppress the combinatorial background in the D_s^- mass spectrum, only the regions of the $D_s^- \to K^+ K^- \pi^-$ Dalitz plot compatible with originating from the $\phi\pi^-$ and $K^{*0}K^-$ decay modes are retained by requiring the K^+K^- mass to be within $20\,\mathrm{MeV}/c^2$ of the known ϕ mass, or the reconstructed $K^+\pi^-$ mass to be within $90\,\mathrm{MeV}/c^2$ of the average $K^*(892)^0$ mass [16]. Possible backgrounds arising from the misidentification of one of the D_s^- decay products are removed with explicit vetoes which apply more stringent PID requirements in a small window of invariant mass of the corresponding particle combination. The main contributions that are removed come from $\overline{\Lambda}_c^- \to K^+\overline{p}\pi^-$, $D^- \to K^+\pi^-\pi^-$, $D_s^- \to K^-\pi^+\pi^-$, and misidentified or partially reconstructed multibody D decays, all originating from semileptonic b-hadron decays.

Due to the small mass difference between the D_s^{*-} and D_s^- mesons, the photon must be emitted close to the D_s^- flight direction. Photons are selected inside a narrow cone surrounding the D_s^- candidate, defined in pseudorapidity and azimuthal angle. Only the highest p_{T} photon inside the cone is combined with the D_s^- candidate. Potential contamination from neutral pions reconstructed as a single merged cluster in the electromagnetic calorimeter is suppressed by employing a neural network classifier trained to separate π^0 mesons from photons [47].

A fit to the $D_s^-\gamma$ invariant-mass distribution, with the reconstructed D_s^- mass constrained to the known value [16], is performed as shown in figure 2. The signal is described by a Gaussian function with a power-law tail on the right hand side of the distribution and the background by an exponential distribution. The power-law tail accounts for cases where additional activity in the calorimeter is mistakenly included in the photon cluster. The *sPlot* technique [48] is employed to subtract the combinatorial background from random photons. Weighted signal is used to create the templates described in section 5. The correlation between the weights and w is below 4%.

The muon candidate is required to have p_{T} in excess of $1.2\,\mathrm{GeV}/c$. Background arising from b-hadrons decaying into final states containing two charmed hadrons, $H_b \to D_s^{*-}H_c$, followed by a semileptonic decay of the charmed hadron $H_c \to \mu^+\nu_\mu X$, where X is one or more hadrons, are suppressed by using a multivariate algorithm based on the isolation of the muon [49]. Finally, the B_s^0 meson candidates are formed by combining μ^+ and D_s^{*-} candidates which are consistent with coming from a common vertex.

5   Signal yield

The signal yield is determined using a template fit to the distribution of the corrected mass [50],

$$m_{\mathrm{corr}} = \sqrt{m_{D_s^{*-}\mu^+}^2 + |p_\perp|^2} + |p_\perp|, \qquad (5.1)$$

where $m_{D_s^{*-}\mu^+}$ is the measured mass of the $D_s^{*-}\mu^+$ candidate, and $p_\perp$ is the momentum of the candidate transverse to the B_s^0 flight direction. When only one massless final-state particle is missing from the decay, m_{corr} peaks at the B_s^0 mass. Only candidates in the range $3500 < m_{\mathrm{corr}} < 5367\,\mathrm{MeV}/c^2$ are considered.

Extended binned maximum-likelihood fits to the m_{corr} distribution are performed independently in seven bins of the reconstructed hadronic recoil, w, to obtain the raw yields
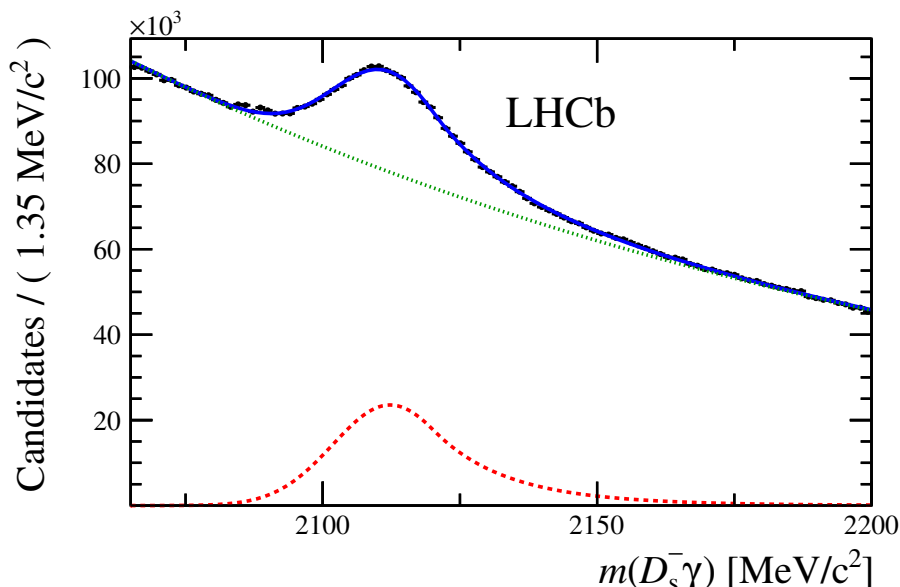
Figure 2. Distribution of the reconstructed $D_s^-\gamma$ mass, $m(D_s^-\gamma)$, with the fit overlaid. The fit is performed constraining the D_s^- mass to the world-average value [16]. The signal and background components are shown separately with dashed red and dotted green lines, respectively.

bin	1	2	3	4	5	6	7
w	1.1087	1.1688	1.2212	1.2717	1.3226	1.3814	1.4667

Table 1. Binning scheme used for this measurement. Only the upper bound for each bin is presented. The lower bound on the first bin corresponds to $w = 1$.

N_{meas} per bin. The binning scheme, detailed in table 1, is chosen such that each w bin has roughly the same signal yield, based on simulation. Obtaining the value of w requires the knowledge of the momentum of the B_s^0 meson, which in the decays under study can be solved up to a quadratic ambiguity. By imposing momentum balance against the visible system with respect to the flight direction, and assuming the mass of the B_s^0 meson, the momentum of the B_s^0 meson can be estimated. To resolve the ambiguity in the solutions, a multivariate regression algorithm based on the flight direction is used [51] yielding a purity on the solutions of around 70%. The m_{corr} distribution is fitted using shapes (templates) of signal and of background distributions mostly obtained from simulation. These simulated decays are selected as described in section 4, and are corrected for the simulation mismodeling as described in section 3.

The largest contribution to the background is due to $B_s^0 \to D_s^{*-}\tau^+\nu_\tau$ decays, with $\tau^- \to \mu^-\overline{\nu}_\mu\nu_\tau$. A small source of background is formed by excited D_s^- mesons decaying into a D_s^{*-} resonance. The only such excited state is the $D_{s1}(2460)^-$ meson, and hence templates for $B_s^0 \to D_{s1}(2460)^-\mu^+\nu_\mu$ and $B_s^0 \to D_{s1}(2460)^-\tau^+\nu_\tau$ decays are included in the fit. The background arising from b hadrons decaying into final states containing two charmed hadrons, $H_b \to D_s^{*-}H_c$, is also addressed. The template for this process is gener-

ated using simulated events of B_s^0, B^0, B^+ and Λ_b^0 decays, with an appropriate admixture of final states, based on their production rates, branching ratios and relative reconstruction efficiencies taken from simulation. The last background considered in the fit is the combinatorial background, arising from random combinations of tracks. This template is obtained from a data sample where the D_s^- meson and the muon have the same charge.

The free parameters in the fit are the signal yield, the relative abundances of $B_s^0 \to D_s^{*-}\tau^+\nu_\tau$ and $B_s^0 \to D_{s1}(2460)^-\mu^+\nu_\mu$ candidates with respect to that of the signal, and the fraction of combinatorial background. The total fraction of backgrounds from $H_c \to \mu^+\nu_\mu X$ decays is fixed to the expected value using the measured branching fractions and selection efficiencies obtained from simulation. A 40% uncertainty is assigned to this component to account for the uncertainties on the branching fractions [16]. The $B_s^0 \to D_{s1}(2460)^-\tau^+\nu_\tau$ contribution is also fixed assuming a value of its ratio with respect to the muonic mode equal to the SM prediction for $\mathcal{B}(B^+ \to D^{*0}\tau^+\nu_\tau)/\mathcal{B}(B^+ \to D^{*0}\mu^+\nu_\mu)$ [21] under the assumption that this ratio is identical for B_s^0 meson decays. The contribution of this decay to the fit is negligible. The Barlow-Beeston "lite" technique [52, 53] is applied to account for the limited size of the simulation samples. The distributions of m_{corr} with the fit overlaid are shown in figure 3.

Using the fractions obtained from the fit, data and simulated distributions of the angular variables $\cos(\theta_\mu)$, $\cos(\theta_{D_s})$, and χ, as defined in section 2, are shown in figure 4. All distributions show good agreement between data and simulation, indicating that integrating over the angles does not introduce biases.

6 Efficiency correction

This analysis requires a precise measurement of all contributions to the efficiency as a function of the true value of the hadronic recoil w_{true} extracted from simulation. However, the overall normalisation of the efficiency is not determined as only its dependency with w_{true} is relevant.

The total efficiency is the product of the geometrical acceptance of the detector, the efficiency of reconstructing all tracks, the trigger requirements, and the full set of kinematic, PID and background rejection requirements. Most of the contributions to the total efficiency are obtained using simulation. Only the particle identification and the D_s^- selection efficiencies are derived from data using control samples. The muon and hadron PID efficiencies are taken from large data samples of $J/\psi \to \mu^+\mu^-$ and $D^{*+} \to D^0\pi^+$ decays, respectively [54]. These samples are then used to determine the PID efficiencies in bins of p, p_{T} and number of tracks in the event. The D_s^- selection efficiency accounts for selecting the regions in the Dalitz plot, as well as the vetoes described in section 4. This efficiency is determined from a sample of fully reconstructed $B_s^0 \to D_s^-\pi^+$ decays as a function of the D_s^- p_{T}. The efficiencies extracted from data are convolved with the simulation to obtain their dependency on w_{true}.

The efficiencies derived from simulation are extracted by comparing the generator-level simulation, based on Pythia [36, 37] and EvtGen [39], to the final reconstructed

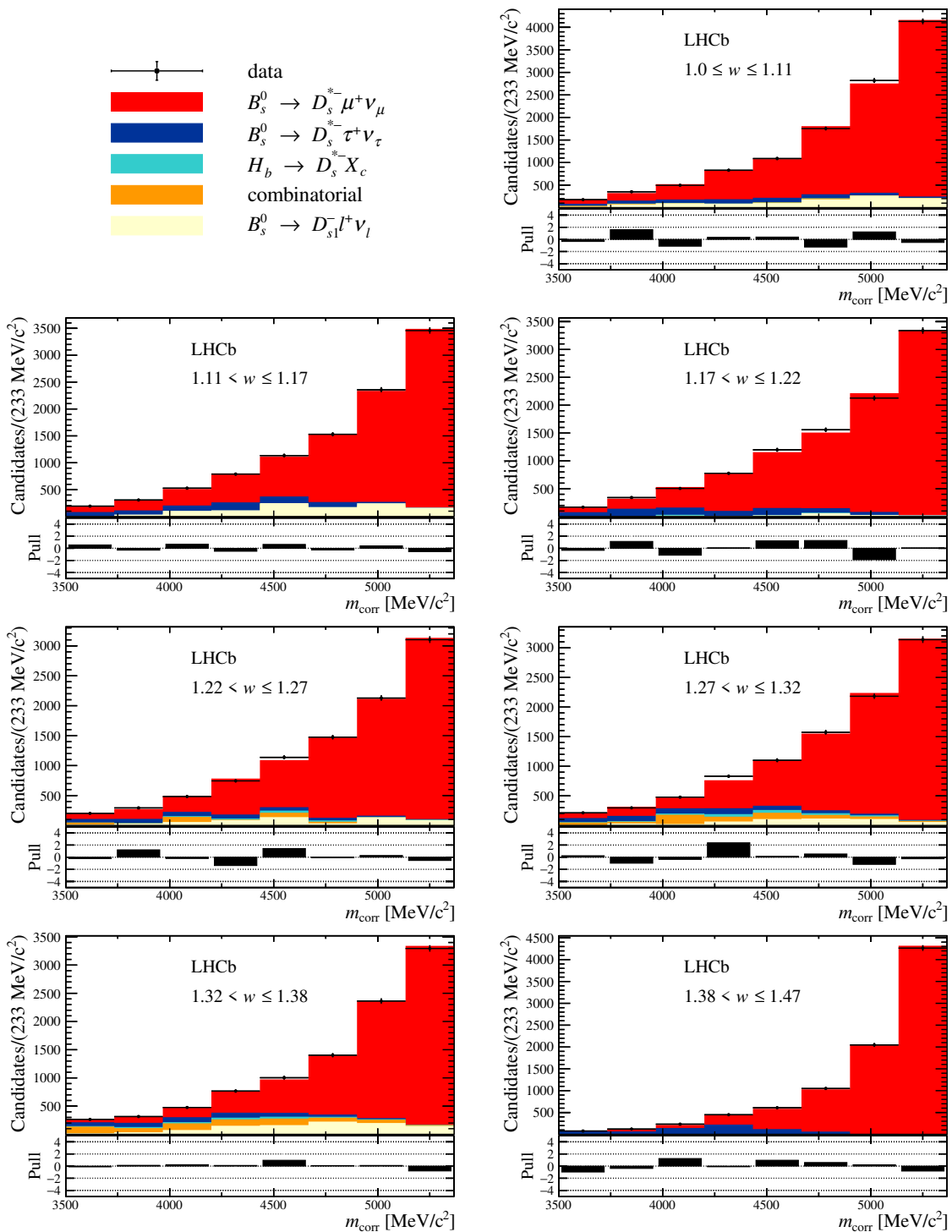**Figure 3**. Distribution of the corrected mass, m_{corr}, for the seven bins of w, overlaid with the fit results. The $B_s^0 \to D_{s1}(2460)^- \tau^+ \nu_\tau$ and the $B_s^0 \to D_{s1}(2460)^- \mu^+ \nu_\mu$ components are combined in $B_s^0 \to D_{s1}(2460)^- \ell^+ \nu_\ell$. Below each plot, differences between the data and fit are shown, normalised by the uncertainty in the data.
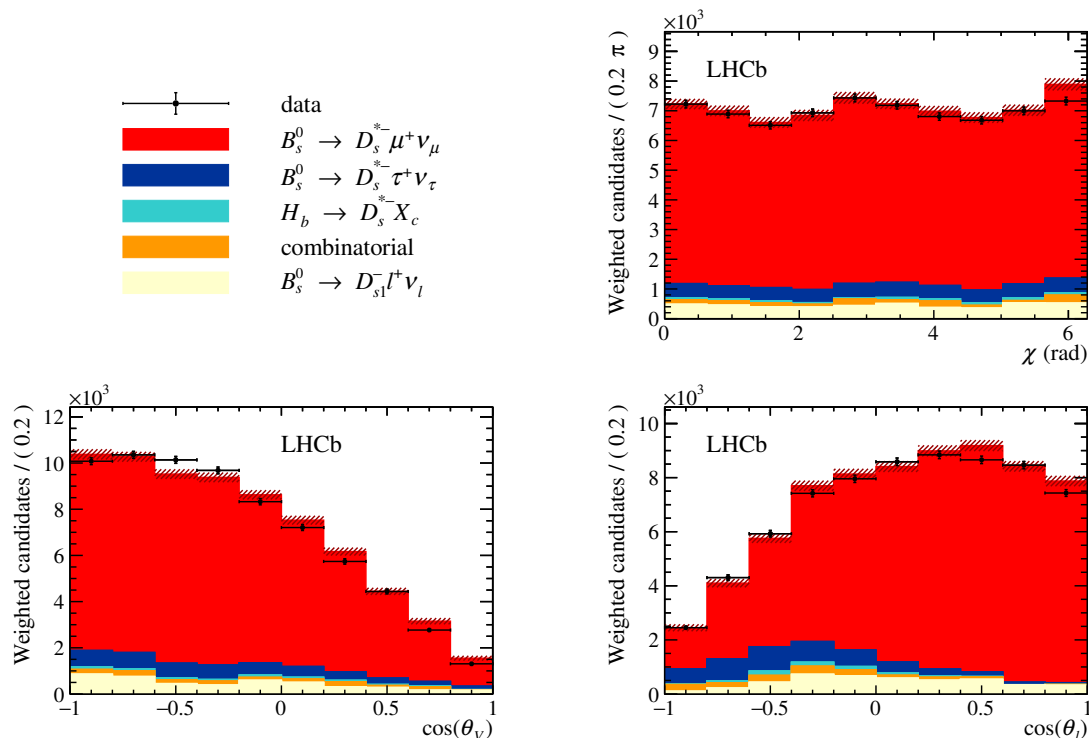
Figure 4. Distribution of (top right) χ, (bottom left) $\cos(\theta_{D_s})$ and (bottom right) $\cos(\theta_\mu)$ integrating over w and the other decay angles from data (black points) compared to the distribution from simulation with their relative size extracted from the fit to the corrected mass. The $B_s^0 \to D_{s1}(2460)^- \tau^+ \nu_\tau$ and the $B_s^0 \to D_{s1}(2460)^- \mu^+ \nu_\mu$ components are combined in $B_s^0 \to D_{s1}(2460)^- \ell^+ \nu_\ell$. The uncertainties on the templates, indicated by the hashed areas in the figures, are a combination from all templates.

and selected simulation sample used for the template fit, omitting the particle identification and the D_s^- selection criteria.

7 Unfolded yields

The measured $B_s^0 \to D_s^{*-} \mu^+ \nu_\mu$ spectrum from section 5 must be unfolded to account for the resolution on the w variable, which is 0.07. The unfolding procedure uses a migration matrix determined from simulation, defined as the probability that a candidate generated in bin j of the w_{true} distribution appears in bin i of the w distribution. The unfolded spectrum is then corrected bin-by-bin using the efficiency described in section 6. The combination of the migration matrix and the total efficiency, called the response matrix, is shown in appendix B.

The unfolding procedure adopted is based on the singular value decomposition (SVD) method [55] using the RooUnfold package implemented in the Root package [56]. The SVD method includes a regularisation procedure that depends upon a parameter k, ranging between unity and the number of degrees of freedom, seven in this case. Using simulation, the optimal value for k is found to be $k = 5$, which minimises the difference between the

yield from the unfolding procedure and the expected yield in each bin. The final yields, labelled $N_{\mathrm{corr}}^{\mathrm{unf}}$, are normalised to unity and presented in table 2.

7.1 Systematic uncertainties

Systematic uncertainties on $N_{\mathrm{corr}}^{\mathrm{unf}}$ originate from the fitted D_s^{*-} and $B_s^0 \to D_s^{*-}\mu^+\nu_\mu$ yields, and the efficiency corrections. By varying the determination of the unfolded yields, systematic uncertainties are quantified. Since this analysis is sensitive only to the shape of the decay distribution and the absolute normalisation is unknown, every such variation is normalised to unity. After normalising, the values are compared to those from the default normalised unfolded yields, and from this the uncertainties are extracted.

The size of the simulated samples, which are very CPU intensive to generate, is the dominating systematic uncertainty on the unfolded yields. The simulated sample size is accounted for in the fit by applying the Barlow-Beeston "lite" technique [52, 53] when determining the signal yield. Its relative contribution to the systematic uncertainty is assessed by not applying this technique and comparing the obtained uncertainties. The uncertainties due to the size of the control samples used to determine the efficiencies and corrections are obtained by varying each of the efficiency and correction inputs within their uncertainty, repeating this 1000 times, and taking the spread as the uncertainty on $N_{\mathrm{corr}}^{\mathrm{unf}}$.

The uncertainty on the SVD unfolding procedure is determined by repeating the regularisation procedure with a different regularisation parameter, k. The nominal value used is $k = 5$, which is changed to $k = 4$ and $k = 6$, and the difference with the nominal value is assigned as the systematic uncertainty.

Two systematic uncertainties are determined to account for assumptions in the simulation. Radiative corrections simulated by the PHOTOS package are known to be incomplete [40, 57]. The difference in $N_{\mathrm{corr}}^{\mathrm{unf}}$ from simulated samples with and without PHOTOS is evaluated and a third of the difference is assigned following ref. [58]. The efficiency due to the detector acceptance, and thus the shape of the efficiency correction, may be affected by the form factors in the HQET model used to generate the simulation, which are based on the 2016 HFLAV averages [59]. This is studied by weighting both the generator level and fully reconstructed simulated samples to the 2019 HFLAV averages [6]: $\rho^2 = 1.122 \pm 0.024$, $R_1(1) = 1.270 \pm 0.026$, and $R_2(1) = 0.852 \pm 0.018$, with correlations $\mathrm{corr}[\rho^2, R_1(1)] = -0.824$, $\mathrm{corr}[\rho^2, R_2(1)] = 0.566$, and $\mathrm{corr}[R_1(1), R_2(1)] = -0.715$. The values of each pair are varied within one standard deviation of their mean, taking into account their correlation. The value of $R_0(1)$ is varied by a 20% uncertainty accounting for finite b- and c-quark masses [21]. These variations result in small changes of the total efficiency and the average difference is taken as the uncertainty.

The effect of the B_s^0 and γ kinematic corrections is assessed by changing the kinematic binning schemes in which the corrections are evaluated. The large effect induced by this change has been checked for statistical fluctuations of the calibration samples. The sample is split randomly into two, after which new corrections and $N_{\mathrm{corr}}^{\mathrm{unf}}$ yields are calculated. No relevant differences between the $N_{\mathrm{corr}}^{\mathrm{unf}}$ values of these two samples are found in any w bin. Hence, the systematic uncertainty is based on the change of binning schemes alone.

	w bin
	1	2	3	4	5	6	7
Fraction of $N_{\mathrm{corr},i}^{\mathrm{unf}}$	0.183	0.144	0.148	0.128	0.117	0.122	0.158
Uncertainties (%)							
Simulation sample size	3.5	3.0	2.8	3.1	3.4	3.0	3.7
Sample sizes for effs and corrections	3.6	3.2	3.0	2.8	2.8	2.7	2.8
SVD unfolding regularisation	0.5	0.5	0.1	0.7	1.2	0.0	0.5
Radiative corrections	0.1	0.2	0.1	0.3	0.4	0.2	0.2
Simulation FF parametrisation	0.3	0.1	0.1	0.1	0.2	0.4	0.2
Kinematic corrections	2.4	1.0	1.1	0.1	0.2	0.1	0.9
Hardware-trigger efficiency	0.3	0.3	0.0	0.2	0.2	0.3	0.1
Software-trigger efficiency	0.0	0.1	0.0	0.0	0.1	0.0	0.0
D_s^- selection efficiency	0.5	0.2	0.3	0.3	0.2	0.1	0.3
Photon background subtraction	0.0	2.3	0.8	2.9	2.0	0.9	0.4
Total systematic uncertainty	5.6	5.1	4.4	5.2	5.0	4.2	4.8
Statistical uncertainty	3.4	2.9	2.7	3.1	3.2	2.9	3.4

Table 2. Fraction of the unfolded yields corrected for the global efficiencies, $N_{\mathrm{corr}}^{\mathrm{unf}}$, for each w bin. Also shown in this table is the breakdown of the systematic and statistical uncertainties on $N_{\mathrm{corr}}^{\mathrm{unf}}$. These are shown as a fraction of the unfolded yield.

The corrections to the hardware and software trigger efficiencies applied to the simulated samples depend on the kinematics and PID of the candidates. The systematic uncertainty is evaluated by changing the binning scheme and the PID selection of the control sample.

The systematic uncertainty due to the kinematic dependence of the D_s^- selection efficiency is assessed by extracting the efficiency as a function of p instead of p_{T} from the $B_s^0 \to D_s^- \pi^+$ control sample.

The systematic uncertainty due to the photon background subtraction, performed through the *sPlot* method with fits to the D_s^{*-} invariant mass, is assessed by implementing the fit with a third-order Chebyshev polynomial for the background description, and repeating the background subtraction process.

Systematic uncertainties induced by the tracking corrections, detector occupancy and PID efficiencies are found to be negligible as they do not affect the corrected mass distribution nor the shape of the efficiency correction.

7.2 Results

The $N_{\mathrm{corr}}^{\mathrm{unf}}$ yields and corresponding systematic and statistical uncertainties per w bin are shown in table 2. The correlations between the $N_{\mathrm{corr}}^{\mathrm{unf}}$ yields including statistical and systematic uncertainties are given in table 3, and the covariance matrix is presented in table 6 in

w bin	1	2	3	4	5	6	7
1	1						
2	0.44	1					
3	0.13	0.60	1				
4	0.19	0.32	0.48	1			
5	0.30	0.30	0.15	0.60	1		
6	0.34	0.38	0.33	0.22	0.54	1	
7	0.27	0.34	0.34	0.27	0.07	0.32	1

Table 3. Correlation matrix for the unfolded data set in bins of w, including both statistical and systematic uncertainties.

appendix B. The detector response combined with the reconstruction efficiency is presented in appendix B. Together these can be used to constrain form-factor parametrisations.

8 Form factor fits

The yields $N_{\rm corr}^{\rm unf}$ with corresponding correlation matrix presented in section 7 can be fit using various form-factor parametrisations. Fits using the commonly used CLN and BGL parametrisations, with the assumptions described in section 2, are presented in the following.

The values of the form-factor parameters are derived from a χ^2 fit with

$$\chi^2 = \sum_{i,j} \left(N_{{\rm corr},i}^{\rm unf} - N_{{\rm exp},i} \right) C_{ij}^{-1} \left(N_{{\rm corr},j}^{\rm unf} - N_{{\rm exp},j} \right). \tag{8.1}$$

In this expression, $N_{{\rm corr},i(j)}^{\rm unf}$ is the normalised, unfolded and efficiency-corrected yield in bin $i(j)$, $N_{{\rm exp},i(j)}$ is the expected yield in bin $i(j)$ obtained from integrating $d\Gamma_{i(j)}/dw$ from the CLN or BGL parametrisation over the bin, and C_{ij} is the covariance matrix describing the statistical uncertainties from the yields and efficiency corrections. This χ^2 function is minimised for the CLN and BGL parametrisations separately. For the CLN parametrisation, the fitted value is $\rho^2 = 1.16 \pm 0.05$, where the uncertainty is only statistical in nature.

For the BGL parametrisation, the unitarity constraint is considered in the minimisation by adding a Gaussian penalty function [60] to the χ^2 defined in eq. (8.1). This function is of the form

$$\theta(U - 1)\left(\frac{U - 1}{\sigma}\right)^2, \tag{8.2}$$

where θ is the Heaviside function, U is the unitarity constraint $\sum_{n=0}^{2}(a_n^f)^2 + \sum_{n=0}^{2}(a_n^{\mathcal{F}_1})^2$, and σ is the theoretical uncertainty associated with the bound [61]. The correlation between the external parameter a_0^f and the fitted parameters a_1^f and a_2^f is not considered due to its small uncertainty. To assess the impact of this choice, the value of a_0^f has been increased (decreased) by $+1(-1)\sigma$. The change in the fitted parameters is observed to be negligible

compared with the overall systematic uncertainty which covers for it for any value of the correlation between a_0^f and the rest of the parameters. This can be explained as a_0^f only enters as a nuisance parameter in the unitarity bounds, which is the only source of correlation between these parameters. As the two scaled parameters a_1^f/a_0^f and a_2^f/a_0^f can be much larger than one (as shown in figure 5) the average magnitude of the correlation diminishes.

The fitted values are $a_1^f = -0.005 \pm 0.034$, and $a_2^f = 1.00^{+0.00}_{-0.19}$, where the uncertainties are only statistical in nature.

8.1 Systematic uncertainties

The systematic uncertainties on the parameters ρ^2, a_1^f and a_2^f originate from the same sources as those described in section 7.1. Additional systematic uncertainties originate from the external parameters used in the form-factor fits. A summary of all systematic uncertainties for ρ^2, a_1^f and a_2^f is shown in table 4.

The impact of changes in signal yields or efficiencies has been assessed by repeating the fit with different conditions and comparing the obtained values to the nominal ones. In the χ^2 fit, the parameters $R_1(1)$ and $R_2(1)$ are fixed to the HFLAV averages [6]. The uncertainties on these values are propagated to the CLN fit outcome by changing $R_1(1)$ and $R_2(1)$ within one standard deviation from their average, while accounting for the correlation between these values. For the BGL fit, the values of the external parameters of the $f(z)$, $g(z)$ and $\mathcal{F}_1(z)$ functions are varied simultaneously within their uncertainty. When the uncertainties are asymmetric the largest is chosen. This process is repeated 1000 times applying the unitarity constraint and the difference between the average of the variations and the nominal value is assigned as a systematic uncertainty.

8.2 Results

An analysis to extract the leading parameters of the form factor describing the semileptonic transition $B_s^0 \to D_s^{*-}\mu^+\nu_\mu$ has been performed. Using the CLN parametrisation the result obtained is

$$\rho^2 = 1.16 \pm 0.05 \,(\text{stat}) \pm 0.07 \,(\text{syst}),$$

where the mass of the muon has not been neglected. To compare with other published results, the fit is repeated assuming a massless muon, resulting in a small shift of the central value of the ρ^2 parameter of about 1.5%, as shown in table 5. The world-average value of ρ^2 for the equivalent $B^0 \to D^{*+}\mu^-\nu_\mu$ decay is $\rho^2 = 1.122 \pm 0.015 \,(\text{stat}) \pm 0.019 \,(\text{syst})$ [6]. Both values of ρ^2 are consistent within their uncertainties. The measurement is also in agreement with the value obtained in ref. [7], $\rho^2 = 1.23 \pm 0.17 \,(\text{stat}) \pm 0.05 \,(\text{syst}) \pm 0.01 \,(\text{ext})$, where the last uncertainty comes from external inputs. That analysis uses $B_s^0 \to D_s^{*-}\mu^+\nu_\mu$ decays from an independent data set, and where the photon from the D_s^{*-} decay is not reconstructed. A comparison with the normalised $\Delta\Gamma/\Delta w$ spectra inferred from the CLN and BGL parametrisations in ref. [7] gives consistent results with the measured w spectrum in this paper, as shown in appendix D.

Source	$\sigma(\rho^2)$	$\sigma(a_1^f)$	$\sigma(a_2^f)$
Simulation sample size	0.053	0.036	$^{+0.00}_{-0.35}$
Sample sizes for efficiencies and corrections	0.020	0.016	$^{+0.00}_{-0.15}$
SVD unfolding regularisation	0.008	0.004	–
Radiative corrections	0.004	–	–
Simulation FF parametrisation	0.007	0.005	–
Kinematic corrections	0.024	0.012	–
Hardware-trigger efficiency	0.001	0.008	–
Software-trigger efficiency	0.004	0.002	–
D_s^- selection efficiency	–	0.008	–
Photon background subtraction	0.002	0.015	–
External parameters in fit	0.024	0.002	$^{+0.00}_{-0.04}$
Total systematic uncertainty	0.068	0.046	$^{+0.00}_{-0.38}$
Statistical uncertainty	0.052	0.034	$^{+0.00}_{-0.19}$

Table 4. Summary of the systematic and statistical uncertainties on the parameters ρ^2, a_1^f and a_2^f from the unfolded CLN and BGL fits. The total systematic uncertainty is obtained by adding the individual components in quadrature.

Using the BGL parametrisation, the results obtained are

$$a_1^f = -0.005 \pm 0.034 \,(\text{stat}) \pm 0.046 \,(\text{syst}),$$
$$a_2^f = 1.00 \,^{+0.00}_{-0.19}\,(\text{stat}) \,^{+0.00}_{-0.38}\,(\text{syst}).$$

In figure 5, the $\Delta\chi^2$ contours for the scaled parameters a_1^f/a_0^f versus a_2^f/a_0^f are shown; figure 8 in appendix C shows the contours of the unscaled a_1^f versus a_2^f parameters. The unitarity constraint results in a non-gaussian distribution of the uncertainty on the a_2^f/a_0^f parameter. The fits to the differential decay rate using both parametrisations are shown in figure 6. The p-values are 8.2% and 1.3% for the CLN and BGL parametrisations, respectively. The low p-values are found to be caused by the third bin in w, which is higher than expected for both parametrisations. When artificially decreasing the central value of this bin by one standard deviation, the p-values increase to 69.7% and 8.3% for the CLN and BGL parametrisations, respectively. The low p-value for the latter fit is explained by the fact that the minimum of the χ^2 function without the unitarity constraint lies in the region excluded by this constraint.

The prediction of the decay rate can also be transformed to a prediction of the expected normalised event yields taking into account the efficiency and resolution, which then is fit to the experimental spectrum. Both procedures provide similar results with small differences induced by slightly different bin-by-bin correlations shown in table 5.
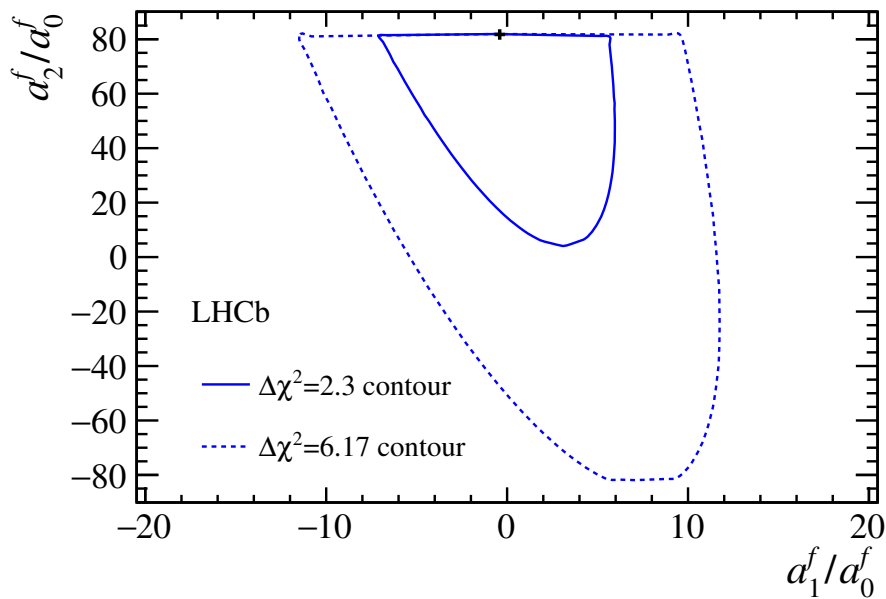
Figure 5. $\Delta\chi^2$ contours for the scaled parameters a_1^f/a_0^f versus a_2^f/a_0^f. The black cross marks the best-fit central value. The solid (dashed) contour encloses the $\Delta\chi^2 = 2.3$ (6.17) region. The observed shape is due to the applied unitarity condition, see eq. (2.11).
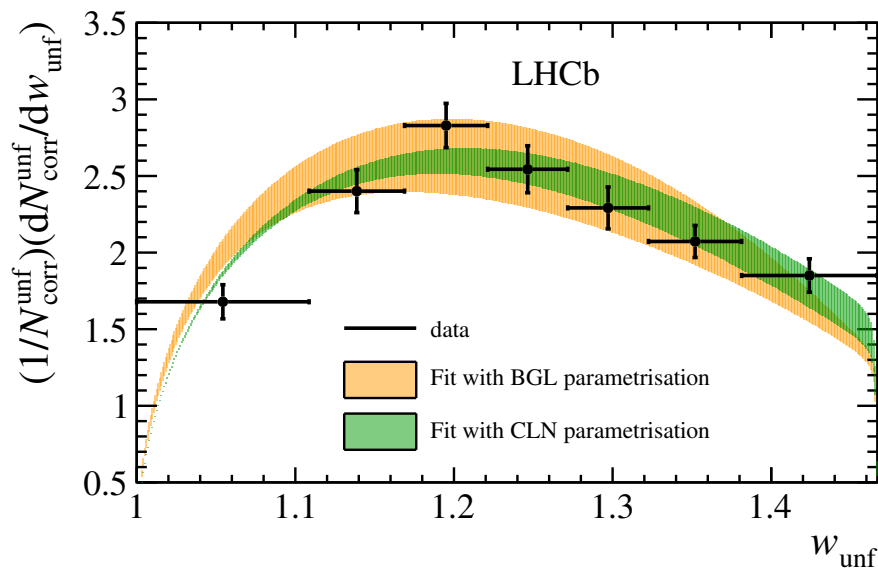

Figure 6. Unfolded normalised differential decay rate with the fit superimposed for the CLN parametrisation (green), and BGL (red). The band in the fit results includes both the statistical and systematic uncertainty on the data yields.

CLN fit	
Unfolded fit	$\rho^2 = 1.16 \pm 0.05 \pm 0.07$
Unfolded fit with massless leptons	$\rho^2 = 1.17 \pm 0.05 \pm 0.07$
Folded fit	$\rho^2 = 1.14 \pm 0.04 \pm 0.07$
BGL fit	
Unfolded fit	$a_1^f = -0.005 \pm 0.034 \pm 0.046$ $a_2^f = 1.00^{+0.00+0.00}_{-0.19-0.38}$
Folded fit	$a_1^f = 0.039 \pm 0.029 \pm 0.046$ $a_2^f = 1.00^{+0.00+0.00}_{-0.13-0.34}$

Table 5. Results from different fit configurations, where the first uncertainty is statistical and the second systematic.

9 Conclusions

In conclusion, this paper presents for the first time the unfolded normalised differential decay rate for $B_s^0 \to D_s^{*-} \mu^+ \nu_\mu$ decays as a function of the recoil parameter w. The unfolded spectrum as a function of w with the systematic uncertainty per bin is given in table 2 and the correlations between these bins in table 3. This result allows to constrain $B_s^0 \to D_s^{*-} \mu^+ \nu_\mu$ form-factor parametrisations. The CLN and BGL form-factor parametrisations have been used to fit the measured spectrum with additional input from $B^0 \to D^{*-} \ell^+ \nu_\ell$ decays. Both fits give consistent results when compared to data.

Figure 7. Total efficiency as a function of w_{true}, including the acceptance of the LHCb detector as well as the reconstruction and selection efficiencies.

A Fitted yields and efficiency

Figure 7 shows the total efficiency applied to the unfolded signal yields, as a function of w_{true}. It is the combination of the reconstruction and selection efficiencies, including the acceptance of the LHCb detector.

B Covariance and response matrices

This section contains the information needed to reproduce a form-factor fit. To perform the fit using the unfolded, efficiency-corrected and normalised yields given in table 2, the corresponding covariance matrix with the combined statistical uncertainties is given in table 6.

To transform theoretical predictions into expected signal yields, the response matrix, given in table 7 is needed. This contains the migration matrix (from the true value of w to the reconstructed one) combined with the reconstruction efficiency. The migration matrix is normalised such that the entries within a given bin of w sum up to unity. The absolute efficiencies have not been measured for this analysis.

w bin $[10^{-5}]$	1	2	3	4	5	6	7
1	16.10						
2	4.73	7.05					
3	1.21	3.81	5.63				
4	1.87	2.12	2.81	6.10			
5	2.74	1.80	0.78	3.37	5.12		
6	2.42	1.82	1.38	0.98	2.17	3.19	
7	3.24	2.69	2.43	2.02	0.44	1.69	8.95

Table 6. Covariance matrix for the unfolded data set in bins of w, including both statistical and systematic uncertainties in units of 10^{-5}.

$[10^{-4}]$	w_{true}						
w	1	2	3	4	5	6	7
1	132.0	29.9	11.0	6.1	2.7	2.4	1.0
2	22.4	111.0	36.3	11.1	5.0	3.8	1.4
3	6.0	28.7	109.0	35.9	12.3	6.6	4.8
4	4.6	9.8	27.0	102.0	34.6	12.3	5.7
5	1.4	4.4	8.9	30.3	98.0	33.7	10.3
6	0.8	0.7	5.0	8.5	34.5	97.0	30.9
7	−0.1	0.7	2.2	5.7	11.0	33.5	98.5

Table 7. Response matrix, containing the migration from w_{true} to w bins together with the total efficiency in units of 10^{-4}.

BGL parameter	Value
a_0^f	0.01221 ± 0.00016
$a_1^{\mathcal{F}_1}$	0.0042 ± 0.0022
$a_2^{\mathcal{F}_1}$	$-0.069^{+0.041}_{-0.037}$
a_0^g	$0.024^{+0.021}_{-0.009}$
a_1^g	$0.05^{+0.39}_{-0.72}$
a_2^g	$1.0^{+0.0}_{-2.0}$
$a_0^{\mathcal{F}_2}$	0.0595 ± 0.0093
$a_1^{\mathcal{F}_2}$	-0.318 ± 0.170

Table 8. Fit inputs used for the BGL fit, taken from ref. [17] and ref. [24].
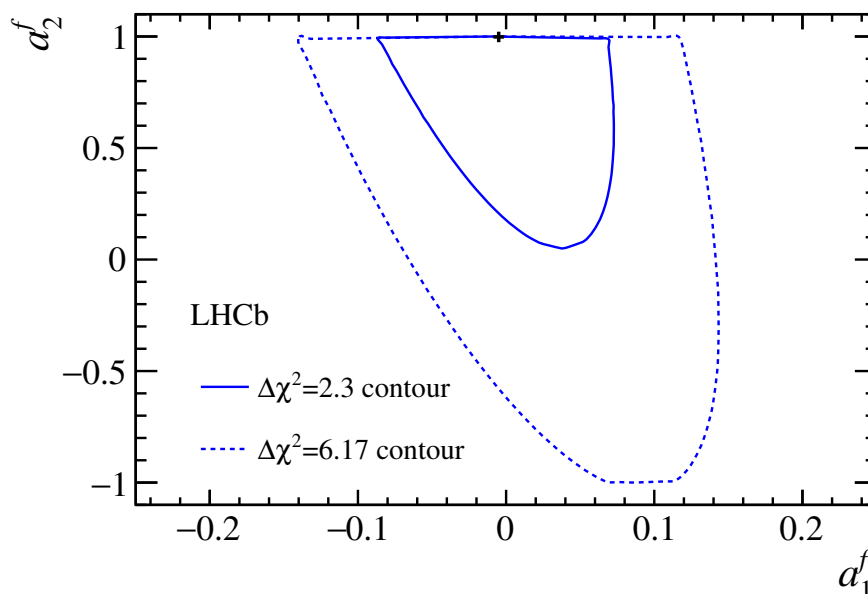
Figure 8. $\Delta\chi^2$ contours for the scaled parameters a_1^f versus a_2^f. The black cross marks the best-fit central value. The solid (dashed) contour encloses the $\Delta\chi^2 = 2.3$ (6.17) region. The observed shape is due to the applied unitarity condition, see eq. (2.11).

C   Additional information BGL fit

Table 8 gives an overview of the fit inputs for the BGL fit. Figure 8 shows the unscaled a_1^f versus a_2^f contours, equivalent to figure 5.
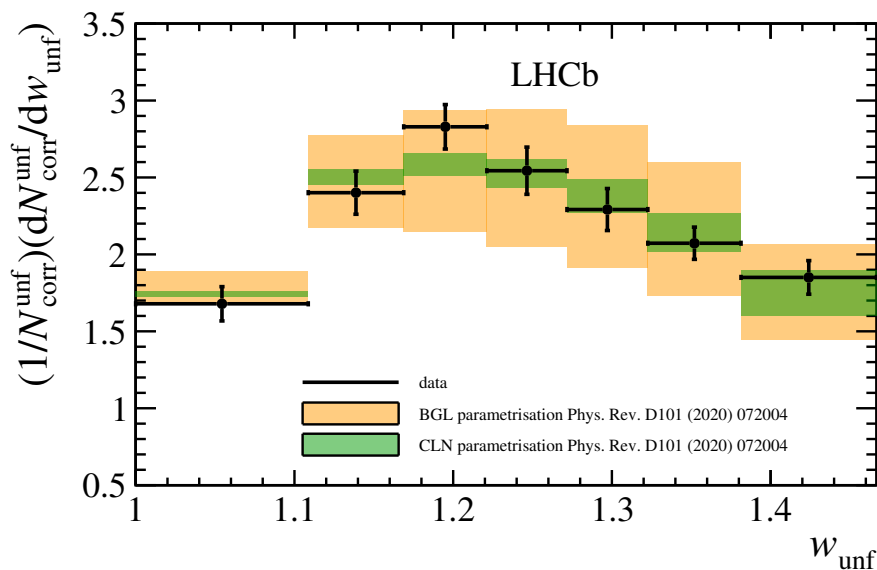
Figure 9. Comparison between the w spectrum measured in this paper to the normalised $\Delta\Gamma/\Delta w$ spectra inferred from the CLN and BGL parametrisations in ref. [7].

D   Comparison with *Phys. Rev. D* **101 (2020) 072004**

The w spectrum measured in this analysis can be compared with the results obtained in ref. [7] where the form-factor parameters of the $B_s^0 \to D_s^{*-}\mu^+\nu_\mu$ decay are measured using a version of the CLN and BGL parametrisations. From this, the normalised $\Delta\Gamma/\Delta w$ spectrum can be inferred, which is shown in figure 9. The spectrum measured in this paper is consistent with the normalised spectra inferred from both CLN and BGL parametrisations used in ref. [7].

Open Access. This article is distributed under the terms of the Creative Commons Attribution License ([CC-BY 4.0](https://creativecommons.org/licenses/by/4.0/)), which permits any use, distribution and reproduction in any medium, provided the original author(s) and source are credited.

References

[1] N. Cabibbo, *Unitary symmetry and leptonic decays*, *Phys. Rev. Lett.* **10** (1963) 531 [INSPIRE].

[2] M. Kobayashi and T. Maskawa, *CP violation in the renormalizable theory of weak interaction*, *Prog. Theor. Phys.* **49** (1973) 652 [INSPIRE].

[3] D. Fakirov and B. Stech, *F and D decays*, *Nucl. Phys. B* **133** (1978) 315 [INSPIRE].

[4] M. Bauer, B. Stech and M. Wirbel, *Exclusive nonleptonic decays of D, D_s, and B mesons*, *Z. Phys. C* **34** (1987) 103 [INSPIRE].

[5] M. Wirbel, B. Stech and M. Bauer, *Exclusive semileptonic decays of heavy mesons*, *Z. Phys. C* **29** (1985) 637 [INSPIRE].

[6] HFLAV collaboration, *Averages of b-hadron, c-hadron, and τ-lepton properties as of* 2018, arXiv:1909.12524 [INSPIRE].

[7] LHCb collaboration, *Measurement of* $|V_{cb}|$ *with* $B_s^0 \to D_s^{(*)-}\mu^+\nu_\mu$ *decays*, *Phys. Rev. D* **101** (2020) 072004 [arXiv:2001.03225] [INSPIRE].

[8] C.J. Monahan, H. Na, C.M. Bouchard, G.P. Lepage and J. Shigemitsu, $B_s \to D_s\ell\nu$ *form factors and the fragmentation fraction ratio* f_s/f_d, *Phys. Rev. D* **95** (2017) 114506 [arXiv:1703.09728] [INSPIRE].

[9] HPQCD collaboration, *Lattice QCD calculation of the* $B_{(s)} \to D_{(s)}^*\ell\nu$ *form factors at zero recoil and implications for* $|V_{cb}|$, *Phys. Rev. D* **97** (2018) 054502 [arXiv:1711.11013] [INSPIRE].

[10] I. Caprini, L. Lellouch and M. Neubert, *Dispersive bounds on the shape of* $B \to D^{(*)}\ell\nu$ *form factors*, *Nucl. Phys. B* **530** (1998) 153 [hep-ph/9712417] [INSPIRE].

[11] C. Boyd, B. Grinstein and R.F. Lebed, *Constraints on form-factors for exclusive semileptonic heavy to light meson decays*, *Phys. Rev. Lett.* **74** (1995) 4603 [hep-ph/9412324] [INSPIRE].

[12] C. Boyd, B. Grinstein and R.F. Lebed, *Model-independent extraction of* $|V_{cb}|$ *using dispersion relations*, *Phys. Lett. B* **353** (1995) 306 [hep-ph/9504235] [INSPIRE].

[13] C. Boyd, B. Grinstein and R.F. Lebed, *Model-independent determinations of* $\bar{B} \to D\ell\nu$, $D^*\ell\nu$ *form factors*, *Nucl. Phys. B* **461** (1996) 493 [hep-ph/9508211] [INSPIRE].

[14] P. Colangelo and F. De Fazio, *Scrutinizing* $\overline{B} \to D^*(D\pi)\ell^-\overline{\nu}_\ell$ *and* $\overline{B} \to D^*(D\gamma)\ell^-\overline{\nu}_\ell$ *in search of new physics footprints*, *JHEP* **06** (2018) 082 [arXiv:1801.10468] [INSPIRE].

[15] A. Sirlin, *Large* m_W, m_Z *behavior of the* $O(\alpha)$ *corrections to semileptonic processes mediated by W*, *Nucl. Phys. B* **196** (1982) 83 [INSPIRE].

[16] PARTICLE DATA GROUP collaboration, *Review of particle physics*, *Phys. Rev. D* **98** (2018) 030001 and 2019 updates [INSPIRE].

[17] P. Gambino, M. Jung and S. Schacht, *The* V_{cb} *puzzle: an update*, *Phys. Lett. B* **795** (2019) 386 [arXiv:1905.08209] [INSPIRE].

[18] A. Kobach, *Continuity and semileptonic* $B_{(s)} \to D_{(s)}$ *form factors*, *Phys. Lett. B* **809** (2020) 135708 [arXiv:1910.13024] [INSPIRE].

[19] M. Bordone, N. Gubernari, D. van Dyk and M. Jung, *Heavy-quark expansion for* $\bar{B}_s \to D_s^{(*)}$ *form factors and unitarity bounds beyond the* $SU(3)_F$ *limit*, *Eur. Phys. J. C* **80** (2020) 347 [arXiv:1912.09335] [INSPIRE].

[20] E. McLean, C.T.H. Davies, A.T. Lytle and J. Koponen, *Lattice QCD form factor for* $B_s \to D_s^*\ell\nu$ *at zero recoil with nonperturbative current renormalisation*, *Phys. Rev. D* **99** (2019) 114512 [arXiv:1904.02046] [INSPIRE].

[21] S. Fajfer, J.F. Kamenik and I. Nišandžić, *On the* $B \to D^*\tau\bar{\nu}_\tau$ *sensitivity to new physics*, *Phys. Rev. D* **85** (2012) 094025 [arXiv:1203.2654] [INSPIRE].

[22] D. Bigi, P. Gambino and S. Schacht, *A fresh look at the determination of* $|V_{cb}|$ *from* $B \to D^*\ell\nu$, *Phys. Lett. B* **769** (2017) 441 [arXiv:1703.06124] [INSPIRE].

[23] B. Grinstein and A. Kobach, *Model-independent extraction of* $|V_{cb}|$ *from* $\bar{B} \to D^*\ell\overline{\nu}$, *Phys. Lett. B* **771** (2017) 359 [arXiv:1703.08170] [INSPIRE].

[24] D. Bigi, P. Gambino and S. Schacht, $R(D^*)$, $|V_{cb}|$, *and the heavy quark symmetry relations between form factors*, *JHEP* **11** (2017) 061 [arXiv:1707.09509] [INSPIRE].

[25] S. Jaiswal, S. Nandi and S.K. Patra, *Updates on extraction of |V_{cb}| and SM prediction of R(D^*) in B → $D^*\ell\nu_\ell$ decays*, *JHEP* **06** (2020) 165 [arXiv:2002.05726] [INSPIRE].

[26] BELLE collaboration, *Precise determination of the CKM matrix element |V_{cb}| with $\bar{B}^0$ → $D^{*+}\ell^-\bar{\nu}_\ell$ decays with hadronic tagging at Belle*, arXiv:1702.01521 [INSPIRE].

[27] BELLE collaboration, *Measurement of the CKM matrix element |V_{cb}| from B^0 → $D^{*-}\ell^+\nu_\ell$ at Belle*, *Phys. Rev. D* **100** (2019) 052007 [arXiv:1809.03290] [INSPIRE].

[28] FLAVOUR LATTICE AVERAGING GROUP collaboration, *FLAG review* 2019, *Eur. Phys. J. C* **80** (2020) 113 [arXiv:1902.08191] [INSPIRE].

[29] LHCb collaboration, *The LHCb detector at the LHC*, 2008 *JINST* **3** S08005 [INSPIRE].

[30] LHCb collaboration, *LHCb detector performance*, *Int. J. Mod. Phys. A* **30** (2015) 1530022 [arXiv:1412.6352] [INSPIRE].

[31] R. Aaij et al., *Performance of the LHCb vertex locator*, 2014 *JINST* **9** P09007 [arXiv:1405.7808] [INSPIRE].

[32] LHCB OUTER TRACKER GROUP collaboration, *Improved performance of the LHCb outer tracker in LHC run* 2, 2017 *JINST* **12** P11016 [arXiv:1708.00819] [INSPIRE].

[33] LHCB RICH GROUP collaboration, *Performance of the LHCb RICH detector at the LHC*, *Eur. Phys. J. C* **73** (2013) 2431 [arXiv:1211.6759] [INSPIRE].

[34] A.A. Alves Jr. et al., *Performance of the LHCb muon system*, 2013 *JINST* **8** P02022 [arXiv:1211.1346] [INSPIRE].

[35] R. Aaij et al., *The LHCb trigger and its performance in* 2011, 2013 *JINST* **8** P04022 [arXiv:1211.3055] [INSPIRE].

[36] T. Sjöstrand, S. Mrenna and P.Z. Skands, *PYTHIA* 6.4 *physics and manual*, *JHEP* **05** (2006) 026 [hep-ph/0603175] [INSPIRE].

[37] T. Sjöstrand, S. Mrenna and P.Z. Skands, *A brief introduction to PYTHIA* 8.1, *Comput. Phys. Commun.* **178** (2008) 852 [arXiv:0710.3820] [INSPIRE].

[38] I. Belyaev et al., *Handling of the generation of primary events in Gauss, the LHCb simulation framework*, *J. Phys. Conf. Ser.* **331** (2011) 032047 [INSPIRE].

[39] D.J. Lange, *The EvtGen particle decay simulation package*, *Nucl. Instrum. Meth. A* **462** (2001) 152 [INSPIRE].

[40] P. Golonka and Z. Was, *PHOTOS Monte Carlo: a precision tool for QED corrections in Z and W decays*, *Eur. Phys. J. C* **45** (2006) 97 [hep-ph/0506026] [INSPIRE].

[41] GEANT4 collaboration, *GEANT4 developments and applications*, *IEEE Trans. Nucl. Sci.* **53** (2006) 270 [INSPIRE].

[42] GEANT4 collaboration, *GEANT4 — a simulation toolkit*, *Nucl. Instrum. Meth. A* **506** (2003) 250 [INSPIRE].

[43] M. Clemencic et al., *The LHCb simulation application, Gauss: design, evolution and experience*, *J. Phys. Conf. Ser.* **331** (2011) 032023 [INSPIRE].

[44] LHCb collaboration, *Measurement of the fragmentation fraction ratio f_s/f_d and its dependence on B meson kinematics*, *JHEP* **04** (2013) 001 [arXiv:1301.5286] [INSPIRE].

[45] LHCb collaboration, *Measurement of f_s/f_u variation with proton-proton collision energy and B-meson kinematics*, *Phys. Rev. Lett.* **124** (2020) 122002 [arXiv:1910.09934] [INSPIRE].

[46] S. Tolk, J. Albrecht, F. Dettori and A. Pellegrino, *Data driven trigger efficiency determination at LHCb*, Tech. Rep. LHCb-PUB-2014-039, CERN, Geneva, Switzerland (2014).

[47] M. Calvo Gomez et al., *A tool for γ/π^0 separation at high energies*, Tech. Rep. LHCb-PUB-2015-016, CERN, Geneva, Switzerland (2015).

[48] M. Pivk and F.R. Le Diberder, *sPlot: a statistical tool to unfold data distributions*, *Nucl. Instrum. Meth. A* **555** (2005) 356 [physics/0402083] [INSPIRE].

[49] LHCb collaboration, *A precise measurement of the B^0 meson oscillation frequency*, *Eur. Phys. J. C* **76** (2016) 412 [arXiv:1604.03475] [INSPIRE].

[50] LHCb collaboration, *Determination of the quark coupling strength $|V_{ub}|$ using baryonic decays*, *Nature Phys.* **11** (2015) 743 [arXiv:1504.01568] [INSPIRE].

[51] G. Ciezarek, A. Lupato, M. Rotondo and M. Vesterinen, *Reconstruction of semileptonically decaying beauty hadrons produced in high energy pp collisions*, *JHEP* **02** (2017) 021 [arXiv:1611.08522] [INSPIRE].

[52] R.J. Barlow and C. Beeston, *Fitting using finite Monte Carlo samples*, *Comput. Phys. Commun.* **77** (1993) 219 [INSPIRE].

[53] K. Cranmer et al., *HistFactory: a tool for creating statistical models for use with RooFit and RooStats*, Tech. Rep. CERN-OPEN-2012-016, New York U., New York, NY, U.S.A. (2012).

[54] L. Anderlini et al., *The PIDCalib package*, Tech. Rep. LHCb-PUB-2016-021, CERN, Geneva, Switzerland (2016).

[55] A. Höcker and V. Kartvelishvili, *SVD approach to data unfolding*, *Nucl. Instrum. Meth. A* **372** (1996) 469 [hep-ph/9509307] [INSPIRE].

[56] T. Adye, *Unfolding algorithms and tests using RooUnfold*, in *PHYSTAT* 2011, CERN-2011-006, CERN, Geneva, Switzerland (2011), pg. 313 [arXiv:1105.1160] [INSPIRE].

[57] S. Calí, S. Klaver, M. Rotondo and B. Sciascia, *Impacts of radiative corrections on measurements of lepton flavour universality in $B \to D\ell\nu_\ell$ decays*, *Eur. Phys. J. C* **79** (2019) 744 [arXiv:1905.02702] [INSPIRE].

[58] BaBar collaboration, *Measurements of the semileptonic decays $\bar{B} \to D\ell\bar{\nu}$ and $\bar{B} \to D^*\ell\bar{\nu}$ using a global fit to $DX\ell\bar{\nu}$ final states*, *Phys. Rev. D* **79** (2009) 012002 [arXiv:0809.0828] [INSPIRE].

[59] HFLAV collaboration, *Averages of b-hadron, c-hadron, and τ-lepton properties as of summer 2016*, *Eur. Phys. J. C* **77** (2017) 895 [arXiv:1612.07233] [INSPIRE].

[60] M. Bordone, M. Jung and D. van Dyk, *Theory determination of $\bar{B} \to D^{(*)}\ell^-\bar{\nu}$ form factors at $O(1/m_c^2)$*, *Eur. Phys. J. C* **80** (2020) 74 [arXiv:1908.09398] [INSPIRE].

[61] D. Bigi and P. Gambino, *Revisiting $B \to D\ell\nu$*, *Phys. Rev. D* **94** (2016) 094008 [arXiv:1606.08030] [INSPIRE].

The LHCb collaboration

R. Aaij[31], C. Abellán Beteta[49], T. Ackernley[59], B. Adeva[45], M. Adinolfi[53], H. Afsharnia[9],
C.A. Aidala[80], S. Aiola[25], Z. Ajaltouni[9], S. Akar[64], P. Albicocco[22], J. Albrecht[14], F. Alessio[47],
M. Alexander[58], A. Alfonso Albero[44], Z. Aliouche[61], G. Alkhazov[37], P. Alvarez Cartelle[60],
A.A. Alves Jr[45], S. Amato[2], Y. Amhis[11], L. An[21], L. Anderlini[21], G. Andreassi[48],
A. Andreianov[37], M. Andreotti[20], F. Archilli[16], A. Artamonov[43], M. Artuso[67], K. Arzymatov[41],
E. Aslanides[10], M. Atzeni[49], B. Audurier[11], S. Bachmann[16], M. Bachmayer[48], J.J. Back[55],
S. Baker[60], P. Baladron Rodriguez[45], V. Balagura[11,b], W. Baldini[20,47], J. Baptista Leite[1],
A. Baranov[41], R.J. Barlow[61], S. Barsuk[11], W. Barter[60], M. Bartolini[23,47,h], F. Baryshnikov[77],
J.M. Basels[13], G. Bassi[28], V. Batozskaya[35], B. Batsukh[67], A. Battig[14], A. Bay[48], M. Becker[14],
F. Bedeschi[28], I. Bediaga[1], A. Beiter[67], L.J. Bel[31], V. Belavin[41], S. Belin[26], V. Bellee[48],
K. Belous[43], I. Belyaev[38], G. Bencivenni[22], E. Ben-Haim[12], S. Benson[31], S. Beranek[13],
A. Berezhnoy[39], R. Bernet[49], D. Berninghoff[16], H.C. Bernstein[67], C. Bertella[47], E. Bertholet[12],
A. Bertolin[27], C. Betancourt[49], F. Betti[19,e], M.O. Bettler[54], Ia. Bezshyiko[49], S. Bhasin[53],
J. Bhom[33], L. Bian[72], M.S. Bieker[14], S. Bifani[52], P. Billoir[12], F.C.R. Bishop[54], A. Bizzeti[21,u],
M. Bjørn[62], M.P. Blago[47], T. Blake[55], F. Blanc[48], S. Blusk[67], D. Bobulska[58], V. Bocci[30],
J.A. Boelhauve[14], O. Boente Garcia[45], T. Boettcher[63], A. Boldyrev[78], A. Bondar[42,x],
N. Bondar[37], S. Borghi[61,47], M. Borisyak[41], M. Borsato[16], J.T. Borsuk[33], S.A. Bouchiba[48],
T.J.V. Bowcock[59], A. Boyer[47], C. Bozzi[20], M.J. Bradley[60], S. Braun[16], A. Brea Rodriguez[45],
M. Brodski[47], J. Brodzicka[33], A. Brossa Gonzalo[55], D. Brundu[26], E. Buchanan[53],
A. Büchler-Germann[49], A. Buonaura[49], C. Burr[47], A. Bursche[26], A. Butkevich[40], J.S. Butter[31],
J. Buytaert[47], W. Byczynski[47], S. Cadeddu[26], H. Cai[72], R. Calabrese[20,g], L. Calero Diaz[22],
S. Cali[22], R. Calladine[52], M. Calvi[24,i], M. Calvo Gomez[44,m], P. Camargo Magalhaes[53],
A. Camboni[44,m], P. Campana[22], D.H. Campora Perez[47], A.F. Campoverde Quezada[5],
S. Capelli[24,i], L. Capriotti[19,e], A. Carbone[19,e], G. Carboni[29], R. Cardinale[23,h], A. Cardini[26],
I. Carli[6], P. Carniti[24,i], K. Carvalho Akiba[31], A. Casais Vidal[45], G. Casse[59], M. Cattaneo[47],
G. Cavallero[47], S. Celani[48], R. Cenci[28], J. Cerasoli[10], A.J. Chadwick[59], M.G. Chapman[53],
M. Charles[12,47], Ph. Charpentier[47], G. Chatzikonstantinidis[52], M. Chefdeville[8], V. Chekalina[41],
C. Chen[3], S. Chen[26], A. Chernov[33], S.-G. Chitic[47], V. Chobanova[45], S. Cholak[48], M. Chrzaszcz[33],
A. Chubykin[37], V. Chulikov[37], P. Ciambrone[22], M.F. Cicala[55], X. Cid Vidal[45], G. Ciezarek[47],
P.E.L. Clarke[57], M. Clemencic[47], H.V. Cliff[54], J. Closier[47], J.L. Cobbledick[61], V. Coco[47],
J.A.B. Coelho[11], J. Cogan[10], E. Cogneras[9], L. Cojocariu[36], P. Collins[47], T. Colombo[47],
A. Comerma-Montells[16], A. Contu[26], N. Cooke[52], G. Coombs[58], S. Coquereau[44], G. Corti[47],
C.M. Costa Sobral[55], B. Couturier[47], D.C. Craik[63], J. Crkovská[66], A. Crocombe[55],
M. Cruz Torres[1,aa], R. Currie[57], C.L. Da Silva[66], E. Dall'Occo[14], J. Dalseno[45,53],
C. D'Ambrosio[47], A. Danilina[38], P. d'Argent[47], A. Davis[61], O. De Aguiar Francisco[47],
K. De Bruyn[47], S. De Capua[61], M. De Cian[48], J.M. De Miranda[1], L. De Paula[2], M. De Serio[18,d],
D. De Simone[49], P. De Simone[22], J.A. de Vries[31], C.T. Dean[66], W. Dean[80], D. Decamp[8],
L. Del Buono[12], B. Delaney[54], H.-P. Dembinski[15], A. Dendek[34], V. Denysenko[49], D. Derkach[78],
O. Deschamps[9], F. Desse[11], F. Dettori[26,f], B. Dey[7], A. Di Canto[47], P. Di Nezza[22], S. Didenko[77],
H. Dijkstra[47], V. Dobishuk[51], A.M. Donohoe[17], F. Dordei[26], M. Dorigo[28,y], A.C. dos Reis[1],
L. Douglas[58], A. Dovbnya[50], A.G. Downes[8], K. Dreimanis[59], M.W. Dudek[33], L. Dufour[47],
G. Dujany[12], P. Durante[47], J.M. Durham[66], D. Dutta[61], M. Dziewiecki[16], A. Dziurda[33],
A. Dzyuba[37], S. Easo[56], U. Egede[69], V. Egorychev[38], S. Eidelman[42,x], S. Eisenhardt[57],
R. Ekelhof[14], S. Ek-In[48], L. Eklund[58], S. Ely[67], A. Ene[36], E. Epple[66], S. Escher[13], J. Eschle[49],
S. Esen[31], T. Evans[47], A. Falabella[19], J. Fan[3], Y. Fan[5], B. Fang[72], N. Farley[52], S. Farry[59],
D. Fazzini[11], P. Fedin[38], M. Féo[47], P. Fernandez Declara[47], A. Fernandez Prieto[45], F. Ferrari[19,e],

L. Ferreira Lopes[48], F. Ferreira Rodrigues[2], S. Ferreres Sole[31], M. Ferrillo[49], M. Ferro-Luzzi[47],
S. Filippov[40], R.A. Fini[18], M. Fiorini[20,g], M. Firlej[34], K.M. Fischer[62], C. Fitzpatrick[47],
T. Fiutowski[34], F. Fleuret[11,b], M. Fontana[47], F. Fontanelli[23,h], R. Forty[47], V. Franco Lima[59],
M. Franco Sevilla[65], M. Frank[47], E. Franzoso[20], G. Frau[16], C. Frei[47], D.A. Friday[58], J. Fu[25,q],
Q. Fuehring[14], W. Funk[47], E. Gabriel[57], T. Gaintseva[41], A. Gallas Torreira[45], D. Galli[19,e],
S. Gallorini[27], S. Gambetta[57], Y. Gan[3], M. Gandelman[2], P. Gandini[25], Y. Gao[4], M. Garau[26],
L.M. Garcia Martin[46], P. Garcia Moreno[44], J. García Pardiñas[49], B. Garcia Plana[45],
F.A. Garcia Rosales[11], L. Garrido[44], D. Gascon[44], C. Gaspar[47], R.E. Geertsema[31], D. Gerick[16],
E. Gersabeck[61], M. Gersabeck[61], T. Gershon[55], D. Gerstel[10], Ph. Ghez[8], V. Gibson[54],
A. Gioventù[45], O.G. Girard[48], P. Gironella Gironell[44], L. Giubega[36], C. Giugliano[20,g],
K. Gizdov[57], V.V. Gligorov[12], C. Göbel[70], E. Golobardes[44,m], D. Golubkov[38], A. Golutvin[60,77],
A. Gomes[1,a], M. Goncerz[33], P. Gorbounov[38,6], I.V. Gorelov[39], C. Gotti[24,i], E. Govorkova[31],
J.P. Grabowski[16], R. Graciani Diaz[44], T. Grammatico[12], L.A. Granado Cardoso[47], E. Graugés[44],
E. Graverini[48], G. Graziani[21], A. Grecu[36], L.M. Greeven[31], R. Greim[31], P. Griffith[20,g],
L. Grillo[61], L. Gruber[47], B.R. Gruberg Cazon[62], C. Gu[3], M. Guarise[20], P. A. Günther[16],
X. Guo[71], E. Gushchin[40], A. Guth[13], Y. Guz[43,47], T. Gys[47], T. Hadavizadeh[62], G. Haefeli[48],
C. Haen[47], S.C. Haines[54], P.M. Hamilton[65], Q. Han[7], X. Han[16], T.H. Hancock[62],
S. Hansmann-Menzemer[16], N. Harnew[62], T. Harrison[59], R. Hart[31], C. Hasse[14], M. Hatch[47],
J. He[5], M. Hecker[60], K. Heijhoff[31], K. Heinicke[14], A.M. Hennequin[47], K. Hennessy[59], L. Henry[46],
J. Heuel[13], A. Hicheur[68], D. Hill[62], M. Hilton[61], S.E. Hollitt[14], P.H. Hopchev[48], J. Hu[16], J. Hu[71],
W. Hu[7], W. Huang[5], X. Huang[72], W. Hulsbergen[31], T. Humair[60], R.J. Hunter[55], M. Hushchyn[78],
D. Hutchcroft[59], D. Hynds[31], P. Ibis[14], M. Idzik[34], D. Ilin[37], P. Ilten[52], A. Inglessi[37], K. Ivshin[37],
R. Jacobsson[47], S. Jakobsen[47], E. Jans[31], B.K. Jashal[46], A. Jawahery[65], V. Jevtic[14], F. Jiang[3],
M. John[62], D. Johnson[47], C.R. Jones[54], T.P. Jones[55], B. Jost[47], N. Jurik[62], S. Kandybei[50],
Y. Kang[3], M. Karacson[47], J.M. Kariuki[53], N. Kazeev[78], M. Kecke[16], F. Keizer[54,47], M. Kelsey[67],
M. Kenzie[55], T. Ketel[32], B. Khanji[47], A. Kharisova[79], S. Kholodenko[43], K.E. Kim[67], T. Kirn[13],
V.S. Kirsebom[48], O. Kitouni[63], S. Klaver[22], K. Klimaszewski[35], S. Koliiev[51], A. Kondybayeva[77],
A. Konoplyannikov[38], P. Kopciewicz[34], R. Kopecna[16], P. Koppenburg[31], M. Korolev[39],
I. Kostiuk[31,51], O. Kot[51], S. Kotriakhova[37,30], P. Kravchenko[37], L. Kravchuk[40], R.D. Krawczyk[47],
M. Kreps[55], F. Kress[60], S. Kretzschmar[13], P. Krokovny[42,x], W. Krupa[34], W. Krzemien[35],
W. Kucewicz[33,l], M. Kucharczyk[33], V. Kudryavtsev[42,x], H.S. Kuindersma[31], G.J. Kunde[66],
T. Kvaratskheliya[38], D. Lacarrere[47], G. Lafferty[61], A. Lai[26], A. Lampis[26], D. Lancierini[49],
J.J. Lane[61], R. Lane[53], G. Lanfranchi[22], C. Langenbruch[13], O. Lantwin[49], T. Latham[55],
F. Lazzari[28,v], C. Lazzeroni[52], R. Le Gac[10], S.H. Lee[80], R. Lefèvre[9], A. Leflat[39], S. Legotin[77],
O. Leroy[10], T. Lesiak[33], B. Leverington[16], H. Li[71], L. Li[62], P. Li[16], P.-R. Li[5], X. Li[66], Y. Li[6],
Y. Li[6], Z. Li[67], X. Liang[67], T. Lin[60], R. Lindner[47], P. Ling[71], V. Lisovskyi[14], R. Litvinov[26],
G. Liu[71], H. Liu[5], S. Liu[6], X. Liu[3], D. Loh[55], A. Loi[26], J. Lomba Castro[45], I. Longstaff[58],
J.H. Lopes[2], G. Loustau[49], G.H. Lovell[54], Y. Lu[6], D. Lucchesi[27,o], S. Luchuk[40],
M. Lucio Martinez[31], V. Lukashenko[31], Y. Luo[3], A. Lupato[27], E. Luppi[20,g], O. Lupton[55],
A. Lusiani[28,t], X. Lyu[5], L. Ma[6], R. Ma[71], S. Maccolini[19,e], F. Machefert[11], F. Maciuc[36],
V. Macko[48], P. Mackowiak[14], S. Maddrell-Mander[53], L.R. Madhan Mohan[53], O. Maev[37,47],
A. Maevskiy[78], D. Maisuzenko[37], M.W. Majewski[34], S. Malde[62], B. Malecki[47], A. Malinin[76],
T. Maltsev[42,x], H. Malygina[16], G. Manca[26,f], G. Mancinelli[10], R. Manera Escalero[44],
D. Manuzzi[19,e], D. Marangotto[25,q], J. Maratas[9,w], J.F. Marchand[8], U. Marconi[19], S. Mariani[21],
C. Marin Benito[11], M. Marinangeli[48], P. Marino[48], J. Marks[16], P.J. Marshall[59], G. Martellotti[30],
L. Martinazzoli[47], M. Martinelli[24,i], D. Martinez Santos[45], F. Martinez Vidal[46], A. Massafferri[1],
M. Materok[13], R. Matev[47], A. Mathad[49], Z. Mathe[47], V. Matiunin[38], C. Matteuzzi[24],
K.R. Mattioli[80], A. Mauri[49], E. Maurice[11,b], M. Mazurek[35], M. McCann[60], L. Mcconnell[17],

T.H. Mcgrath[61], A. McNab[61], R. McNulty[17], J.V. Mead[59], B. Meadows[64], C. Meaux[10],
G. Meier[14], N. Meinert[74], D. Melnychuk[35], S. Meloni[24,i], M. Merk[31], A. Merli[25],
L. Meyer Garcia[2], M. Mikhasenko[47], D.A. Milanes[73], E. Millard[55], M.-N. Minard[8], O. Mineev[38],
L. Minzoni[20,g], S.E. Mitchell[57], B. Mitreska[61], D.S. Mitzel[47], A. Mödden[14], A. Mogini[12],
R.A. Mohammed[62], R.D. Moise[60], T. Mombächer[14], I.A. Monroy[73], S. Monteil[9], M. Morandin[27],
G. Morello[22], M.J. Morello[28,t], J. Moron[34], A.B. Morris[10], A.G. Morris[55], R. Mountain[67],
H. Mu[3], F. Muheim[57], M. Mukherjee[7], M. Mulder[47], D. Müller[47], K. Müller[49], C.H. Murphy[62],
D. Murray[61], P. Muzzetto[26], P. Naik[53], T. Nakada[48], R. Nandakumar[56], T. Nanut[48], I. Nasteva[2],
M. Needham[57], I. Neri[20,g], N. Neri[25,q], S. Neubert[16], N. Neufeld[47], R. Newcombe[60],
T.D. Nguyen[48], C. Nguyen-Mau[48,n], E.M. Niel[11], S. Nieswand[13], N. Nikitin[39], N.S. Nolte[47],
C. Nunez[80], A. Oblakowska-Mucha[34], V. Obraztsov[43], S. Ogilvy[58], D.P. O'Hanlon[53],
R. Oldeman[26,f], C.J.G. Onderwater[75], J. D. Osborn[80], A. Ossowska[33], J.M. Otalora Goicochea[2],
T. Ovsiannikova[38], P. Owen[49], A. Oyanguren[46], B. Pagare[55], P.R. Pais[48], T. Pajero[28,t],
A. Palano[18], M. Palutan[22], Y. Pan[61], G. Panshin[79], A. Papanestis[56], M. Pappagallo[57],
L.L. Pappalardo[20,g], C. Pappenheimer[64], W. Parker[65], C. Parkes[61], B. Passalacqua[20],
G. Passaleva[21,47], A. Pastore[18], M. Patel[60], C. Patrignani[19,e], A. Pearce[47], A. Pellegrino[31],
M. Pepe Altarelli[47], S. Perazzini[19], D. Pereima[38], P. Perret[9], L. Pescatore[48], K. Petridis[53],
A. Petrolini[23,h], A. Petrov[76], S. Petrucci[57], M. Petruzzo[25,q], A. Philippov[41], L. Pica[28],
B. Pietrzyk[8], G. Pietrzyk[48], M. Pili[62], D. Pinci[30], J. Pinzino[47], F. Pisani[19], A. Piucci[16], Resmi
P.K[10], V. Placinta[36], S. Playfer[57], J. Plews[52], M. Plo Casasus[45], F. Polci[12], M. Poli Lener[22],
M. Poliakova[67], A. Poluektov[10], N. Polukhina[77,c], I. Polyakov[67], E. Polycarpo[2], G.J. Pomery[53],
S. Ponce[47], A. Popov[43], D. Popov[52], S. Popov[41], S. Poslavskii[43], K. Prasanth[33], L. Promberger[47],
C. Prouve[45], V. Pugatch[51], A. Puig Navarro[49], H. Pullen[62], G. Punzi[28,p], W. Qian[5], J. Qin[5],
R. Quagliani[12], B. Quintana[8], N.V. Raab[17], R.I. Rabadan Trejo[10], B. Rachwal[34],
J.H. Rademacker[53], M. Rama[28], M. Ramos Pernas[45], M.S. Rangel[2], F. Ratnikov[41,78], G. Raven[32],
M. Reboud[8], F. Redi[48], F. Reiss[12], C. Remon Alepuz[46], Z. Ren[3], V. Renaudin[62], R. Ribatti[28],
S. Ricciardi[56], D.S. Richards[56], S. Richards[53], K. Rinnert[59], P. Robbe[11], A. Robert[12],
G. Robertson[57], A.B. Rodrigues[48], E. Rodrigues[64], J.A. Rodriguez Lopez[73], M. Roehrken[47],
S. Roiser[47], A. Rollings[62], V. Romanovskiy[43], M. Romero Lamas[45], A. Romero Vidal[45],
J.D. Roth[80], M. Rotondo[22], M.S. Rudolph[67], T. Ruf[47], J. Ruiz Vidal[46], A. Ryzhikov[78],
J. Ryzka[34], J.J. Saborido Silva[45], N. Sagidova[37], N. Sahoo[55], B. Saitta[26,f], C. Sanchez Gras[31],
C. Sanchez Mayordomo[46], R. Santacesaria[30], C. Santamarina Rios[45], M. Santimaria[22],
E. Santovetti[29,j], D. Saranin[77], G. Sarpis[61], M. Sarpis[16], A. Sarti[30], C. Satriano[30,s], A. Satta[29],
M. Saur[5], D. Savrina[38,39], H. Sazak[9], L.G. Scantlebury Smead[62], S. Schael[13], M. Schellenberg[14],
M. Schiller[58], H. Schindler[47], M. Schmelling[15], T. Schmelzer[14], B. Schmidt[47], O. Schneider[48],
A. Schopper[47], H.F. Schreiner[64], M. Schubiger[31], S. Schulte[48], M.H. Schune[11], R. Schwemmer[47],
B. Sciascia[22], A. Sciubba[30,k], S. Sellam[68], A. Semennikov[38], A. Sergi[52,47], N. Serra[49],
J. Serrano[10], L. Sestini[27], A. Seuthe[14], P. Seyfert[47], D.M. Shangase[80], M. Shapkin[43],
I. Shchemerov[77], L. Shchutska[48], T. Shears[59], L. Shekhtman[42,x], Z. Shen[4], V. Shevchenko[76,77],
E.B. Shields[24,i], E. Shmanin[77], J.D. Shupperd[67], B.G. Siddi[20], R. Silva Coutinho[49],
L. Silva de Oliveira[2], G. Simi[27,o], S. Simone[18,d], I. Skiba[20,g], N. Skidmore[16], T. Skwarnicki[67],
M.W. Slater[52], J.C. Smallwood[62], J.G. Smeaton[54], A. Smetkina[38], E. Smith[13], I.T. Smith[57],
M. Smith[60], A. Snoch[31], M. Soares[19], L. Soares Lavra[9], M.D. Sokoloff[64], F.J.P. Soler[58],
A. Solovev[37], I. Solovyev[37], F.L. Souza De Almeida[2], B. Souza De Paula[2], B. Spaan[14],
E. Spadaro Norella[25,q], P. Spradlin[58], F. Stagni[47], M. Stahl[64], S. Stahl[47], P. Stefko[48],
O. Steinkamp[49], S. Stemmle[16], O. Stenyakin[43], M. Stepanova[37], H. Stevens[14], S. Stone[67],
M.E. Stramaglia[48], M. Straticiuc[36], D. Strekalina[77], S. Strokov[79], F. Suljik[62], J. Sun[26], L. Sun[72],
Y. Sun[65], P. Svihra[61], P.N. Swallow[52], K. Swientek[34], A. Szabelski[35], T. Szumlak[34],

M. Szymanski[47], S. Taneja[61], Z. Tang[3], T. Tekampe[14], F. Teubert[47], E. Thomas[47],
K.A. Thomson[59], M.J. Tilley[60], V. Tisserand[9], S. T'Jampens[8], M. Tobin[6], S. Tolk[47],
L. Tomassetti[20,g], D. Tonelli[28], D. Torres Machado[1], D.Y. Tou[12], E. Tournefier[8], M. Traill[58],
M.T. Tran[48], E. Trifonova[77], C. Trippl[48], A. Trisovic[54], A. Tsaregorodtsev[10], G. Tuci[28,47,p],
A. Tully[48], N. Tuning[31], A. Ukleja[35], D.J. Unverzagt[16], A. Usachov[31], A. Ustyuzhanin[41,78],
U. Uwer[16], A. Vagner[79], V. Vagnoni[19], A. Valassi[47], G. Valenti[19], M. van Beuzekom[31],
H. Van Hecke[66], E. van Herwijnen[47], C.B. Van Hulse[17], M. van Veghel[75], R. Vazquez Gomez[44,22],
P. Vazquez Regueiro[45], C. Vázquez Sierra[31], S. Vecchi[20], J.J. Velthuis[53], M. Veltri[21,r],
A. Venkateswaran[67], M. Vernet[9], M. Veronesi[31], M. Vesterinen[55], J.V. Viana Barbosa[47],
D. Vieira[64], M. Vieites Diaz[48], H. Viemann[74], X. Vilasis-Cardona[44], E. Vilella Figueras[59],
P. Vincent[12], G. Vitali[28], A. Vitkovskiy[31], A. Vollhardt[49], D. Vom Bruch[12], A. Vorobyev[37],
V. Vorobyev[42,x], N. Voropaev[37], R. Waldi[74], J. Walsh[28], C. Wang[16], J. Wang[3], J. Wang[72],
J. Wang[4], J. Wang[6], M. Wang[3], R. Wang[53], Y. Wang[7], Z. Wang[49], D.R. Ward[54], H.M. Wark[59],
N.K. Watson[52], S.G. Weber[12], D. Websdale[60], A. Weiden[49], C. Weisser[63], B.D.C. Westhenry[53],
D.J. White[61], M. Whitehead[13], D. Wiedner[14], G. Wilkinson[62], M. Wilkinson[67], I. Williams[54],
M. Williams[63], M.R.J. Williams[61], T. Williams[52], F.F. Wilson[56], W. Wislicki[35], M. Witek[33],
L. Witola[16], G. Wormser[11], S.A. Wotton[54], H. Wu[67], K. Wyllie[47], Z. Xiang[5], D. Xiao[7], Y. Xie[7],
H. Xing[71], A. Xu[4], J. Xu[5], L. Xu[3], M. Xu[7], Q. Xu[5], Z. Xu[4], D. Yang[3], Y. Yang[5], Z. Yang[3],
Z. Yang[65], Y. Yao[67], L.E. Yeomans[59], H. Yin[7], J. Yu[7,z], X. Yuan[67], O. Yushchenko[43],
K.A. Zarebski[52], M. Zavertyaev[15,c], M. Zdybal[33], O. Zenaiev[47], M. Zeng[3], D. Zhang[7], L. Zhang[3],
S. Zhang[4], W.C. Zhang[3], Y. Zhang[47], A. Zhelezov[16], Y. Zheng[5], X. Zhou[5], Y. Zhou[5], X. Zhu[3],
V. Zhukov[13,39], J.B. Zonneveld[57], S. Zucchelli[19,e], D. Zuliani[27] and G. Zunica[61]

1 Centro Brasileiro de Pesquisas Físicas (CBPF), Rio de Janeiro, Brazil
2 Universidade Federal do Rio de Janeiro (UFRJ), Rio de Janeiro, Brazil
3 Center for High Energy Physics, Tsinghua University, Beijing, China
4 School of Physics State Key Laboratory of Nuclear Physics and Technology, Peking University, Beijing, China
5 University of Chinese Academy of Sciences, Beijing, China
6 Institute Of High Energy Physics (IHEP), Beijing, China
7 Institute of Particle Physics, Central China Normal University, Wuhan, Hubei, China
8 Univ. Grenoble Alpes, Univ. Savoie Mont Blanc, CNRS, IN2P3-LAPP, Annecy, France
9 Université Clermont Auvergne, CNRS/IN2P3, LPC, Clermont-Ferrand, France
10 Aix Marseille Univ, CNRS/IN2P3, CPPM, Marseille, France
11 Université Paris-Saclay, CNRS/IN2P3, IJCLab, Orsay, France
12 LPNHE, Sorbonne Université, Paris Diderot Sorbonne Paris Cité, CNRS/IN2P3, Paris, France
13 I. Physikalisches Institut, RWTH Aachen University, Aachen, Germany
14 Fakultät Physik, Technische Universität Dortmund, Dortmund, Germany
15 Max-Planck-Institut für Kernphysik (MPIK), Heidelberg, Germany
16 Physikalisches Institut, Ruprecht-Karls-Universität Heidelberg, Heidelberg, Germany
17 School of Physics, University College Dublin, Dublin, Ireland
18 INFN Sezione di Bari, Bari, Italy
19 INFN Sezione di Bologna, Bologna, Italy
20 INFN Sezione di Ferrara, Ferrara, Italy
21 INFN Sezione di Firenze, Firenze, Italy
22 INFN Laboratori Nazionali di Frascati, Frascati, Italy
23 INFN Sezione di Genova, Genova, Italy
24 INFN Sezione di Milano-Bicocca, Milano, Italy
25 INFN Sezione di Milano, Milano, Italy
26 INFN Sezione di Cagliari, Monserrato, Italy

27 *Universita degli Studi di Padova, Universita e INFN, Padova, Padova, Italy*

28 *INFN Sezione di Pisa, Pisa, Italy*

29 *INFN Sezione di Roma Tor Vergata, Roma, Italy*

30 *INFN Sezione di Roma La Sapienza, Roma, Italy*

31 *Nikhef National Institute for Subatomic Physics, Amsterdam, Netherlands*

32 *Nikhef National Institute for Subatomic Physics and VU University Amsterdam, Amsterdam, Netherlands*

33 *Henryk Niewodniczanski Institute of Nuclear Physics Polish Academy of Sciences, Kraków, Poland*

34 *AGH — University of Science and Technology, Faculty of Physics and Applied Computer Science, Kraków, Poland*

35 *National Center for Nuclear Research (NCBJ), Warsaw, Poland*

36 *Horia Hulubei National Institute of Physics and Nuclear Engineering, Bucharest-Magurele, Romania*

37 *Petersburg Nuclear Physics Institute NRC Kurchatov Institute (PNPI NRC KI), Gatchina, Russia*

38 *Institute of Theoretical and Experimental Physics NRC Kurchatov Institute (ITEP NRC KI), Moscow, Russia*

39 *Institute of Nuclear Physics, Moscow State University (SINP MSU), Moscow, Russia*

40 *Institute for Nuclear Research of the Russian Academy of Sciences (INR RAS), Moscow, Russia*

41 *Yandex School of Data Analysis, Moscow, Russia*

42 *Budker Institute of Nuclear Physics (SB RAS), Novosibirsk, Russia*

43 *Institute for High Energy Physics NRC Kurchatov Institute (IHEP NRC KI), Protvino, Russia, Protvino, Russia*

44 *ICCUB, Universitat de Barcelona, Barcelona, Spain*

45 *Instituto Galego de Física de Altas Enerxías (IGFAE), Universidade de Santiago de Compostela, Santiago de Compostela, Spain*

46 *Instituto de Fisica Corpuscular, Centro Mixto Universidad de Valencia — CSIC, Valencia, Spain*

47 *European Organization for Nuclear Research (CERN), Geneva, Switzerland*

48 *Institute of Physics, Ecole Polytechnique Fédérale de Lausanne (EPFL), Lausanne, Switzerland*

49 *Physik-Institut, Universität Zürich, Zürich, Switzerland*

50 *NSC Kharkiv Institute of Physics and Technology (NSC KIPT), Kharkiv, Ukraine*

51 *Institute for Nuclear Research of the National Academy of Sciences (KINR), Kyiv, Ukraine*

52 *University of Birmingham, Birmingham, United Kingdom*

53 *H.H. Wills Physics Laboratory, University of Bristol, Bristol, United Kingdom*

54 *Cavendish Laboratory, University of Cambridge, Cambridge, United Kingdom*

55 *Department of Physics, University of Warwick, Coventry, United Kingdom*

56 *STFC Rutherford Appleton Laboratory, Didcot, United Kingdom*

57 *School of Physics and Astronomy, University of Edinburgh, Edinburgh, United Kingdom*

58 *School of Physics and Astronomy, University of Glasgow, Glasgow, United Kingdom*

59 *Oliver Lodge Laboratory, University of Liverpool, Liverpool, United Kingdom*

60 *Imperial College London, London, United Kingdom*

61 *Department of Physics and Astronomy, University of Manchester, Manchester, United Kingdom*

62 *Department of Physics, University of Oxford, Oxford, United Kingdom*

63 *Massachusetts Institute of Technology, Cambridge, MA, United States*

64 *University of Cincinnati, Cincinnati, OH, United States*

65 *University of Maryland, College Park, MD, United States*

66 *Los Alamos National Laboratory (LANL), Los Alamos, United States*

67 *Syracuse University, Syracuse, NY, United States*

68 *Laboratory of Mathematical and Subatomic Physics , Constantine, Algeria, associated to [2]*

69 *School of Physics and Astronomy, Monash University, Melbourne, Australia, associated to [55]*

70 *Pontifícia Universidade Católica do Rio de Janeiro (PUC-Rio), Rio de Janeiro, Brazil, associated to [2]*

71   *Guangdong Provencial Key Laboratory of Nuclear Science, Institute of Quantum Matter, South China Normal University, Guangzhou, China, associated to* [3]

72   *School of Physics and Technology, Wuhan University, Wuhan, China, associated to* [3]

73   *Departamento de Fisica , Universidad Nacional de Colombia, Bogota, Colombia, associated to* [12]

74   *Institut für Physik, Universität Rostock, Rostock, Germany, associated to* [16]

75   *Van Swinderen Institute, University of Groningen, Groningen, Netherlands, associated to* [31]

76   *National Research Centre Kurchatov Institute, Moscow, Russia, associated to* [38]

77   *National University of Science and Technology "MISIS", Moscow, Russia, associated to* [38]

78   *National Research University Higher School of Economics, Moscow, Russia, associated to* [41]

79   *National Research Tomsk Polytechnic University, Tomsk, Russia, associated to* [38]

80   *University of Michigan, Ann Arbor, United States, associated to* [67]

a   *Universidade Federal do Triângulo Mineiro (UFTM), Uberaba-MG, Brazil*

b   *Laboratoire Leprince-Ringuet, Palaiseau, France*

c   *P.N. Lebedev Physical Institute, Russian Academy of Science (LPI RAS), Moscow, Russia*

d   *Università di Bari, Bari, Italy*

e   *Università di Bologna, Bologna, Italy*

f   *Università di Cagliari, Cagliari, Italy*

g   *Università di Ferrara, Ferrara, Italy*

h   *Università di Genova, Genova, Italy*

i   *Università di Milano Bicocca, Milano, Italy*

j   *Università di Roma Tor Vergata, Roma, Italy*

k   *Università di Roma La Sapienza, Roma, Italy*

l   *AGH — University of Science and Technology, Faculty of Computer Science, Electronics and Telecommunications, Kraków, Poland*

m   *DS4DS, La Salle, Universitat Ramon Llull, Barcelona, Spain*

n   *Hanoi University of Science, Hanoi, Vietnam*

o   *Università di Padova, Padova, Italy*

p   *Università di Pisa, Pisa, Italy*

q   *Università degli Studi di Milano, Milano, Italy*

r   *Università di Urbino, Urbino, Italy*

s   *Università della Basilicata, Potenza, Italy*

t   *Scuola Normale Superiore, Pisa, Italy*

u   *Università di Modena e Reggio Emilia, Modena, Italy*

v   *Università di Siena, Siena, Italy*

w   *MSU — Iligan Institute of Technology (MSU-IIT), Iligan, Philippines*

x   *Novosibirsk State University, Novosibirsk, Russia*

y   *INFN Sezione di Trieste, Trieste, Italy*

z   *Physics and Micro Electronic College, Hunan University, Changsha City, China*

aa   *Universidad Nacional Autonoma de Honduras, Tegucigalpa, Honduras*